Optimal Power Management of Interconnected Microgrids Using Virtual Inertia Control Technique

Mahmoud Elshenawy [1], Ashraf Fahmy [2,*], Adel Elsamahy [1,3], Shaimaa. A. Kandil [1] and Helmy M. El Zoghby [1]

[1] Electrical Power and Machines Engineering Department, Faculty of Engineering, Helwan University, Cairo 11792, Egypt
[2] Faculty of Science and Engineering, Swansea University, Wales SA1 8EN, UK
[3] Academy of Scientific Research and Technology (ASRT), Cairo 11792, Egypt
[*] Correspondence: a.a.fahmy@swansea.ac.uk

Abstract: Two interconnected AC microgrids are proposed based on three renewable energy sources (RESs): wind, solar, and biogas. The wind turbine drives a permanent magnet synchronous generator (PMSG). A solar photovoltaic system (SPVS) with an appropriate inverter was incorporated. The biogas genset (BG) consists of a biogas engine coupled with a synchronous generator. Two interconnected AC microgrids, M_1 and M_2, were considered for study in this work. The microgrid M_2 is connected to a diesel engine (DE) characterized by a continuous power supply. The distribution power loss of the interconnected AC microgrids comprises in line loss. The M_1 and M_2 losses are modeled as an objective function (OF). The power quality enhancement of the interconnected microgrids will be achieved by minimizing this OF. This research also created a unique frequency control method called virtual inertia control (VIC), which stabilizes the microgrid frequency using an optimal controller. In this paper, the following five controllers are studied: a proportional integral controller (PI), a fractional order PI controller (FOPI), a fuzzy PI controller (FPI), a fuzzy fractional order PI controller (FFOPI), and a VIC based on FFOPI controller. The five controllers were tuned using particle swarm optimization (PSO) to minimize the (OF). The main contribution of this paper is the comprehensive study of the performance of interconnected AC microgrids under step load disturbances, step changes in wind/solar input power, and eventually grid following/forming contingencies as well as the virtual inertia control of renewable energy resources used in the structure of the microgrids.

Keywords: contingency of power system; energy storage system (ESS); fuzzy fractional order PI (FFOPI); fuzzy PI (FPI); multi-objective optimization; microgrid; power quality enhancement; particle swarm optimization (PSO); virtual inertia control

1. Introduction

The rapid growth of renewable energy sources (RESs) in recent years has been attributed to the growing concerns about environmental factors, greenhouse gases (particularly CO_2), and global warming. As a result, numerous issues with the integration of renewable energy into networks as well as their solutions have been discussed in the literature. The primary traits of RESs that make it difficult to integrate them with the grid and the load are the intermittent availability of the input source, which results in extremely intermittent power, inconsistent power output and low flux density, meaning they require more space per unit of power generation than conventional generators, and low inertia.

RESs, such as SPVSs (solar photovoltaic systems) and WECSs (wind energy conversion systems), have lower inertia than conventional sources, limiting the grid's potential to improve stability.

Various integrations of RES sources and their data have been discussed in the literature. The stability of microgrids is of particular interest. Many authors [1] have discussed and introduced some aspects of microgrids in the literature. Sustained low frequency deviations, as studied in [2–4], are one of the problems in microgrids. Another issue in microgrid systems is voltage control [5,6]. There is literature that solves these problems separately and jointly. Because of the intermittent nature of solar and wind power, a backup is required. One of the proposals made in [7,8] is inverter-connected battery backup. The other option is a connected diesel/biogas power plant [9]. In a wind-solar-a diesel system, many control strategies are implemented using various optimizing techniques [10–12]. Some proposals on AC and DC microgrids have been made [13,14]. Furthermore, the rate of generation deviation in SPVS is extremely high due to cloud changes [15]. An inverter connects the SPVS's PV plant to the power system. As a result, control of the PV unit is provided by inverter control [16].

Due to its aerodynamic properties, a wind turbine's output power is proportional to the square of the rotor diameter and the cube of the wind speed [17]. In WECSs, a permanent magnet synchronous generator (PMSG) is frequently used. PMSGs, however, are reliable and do not require a separate field control system [18]. Power inverters connect SPVSs and WECSs to the point of common coupling (PCC). Additionally, the network receives virtual inertia from the associated inverter [19]. There is literature that demonstrates how the virtual inertia of WECSs and SPVSs, which is based on inverters, can almost act as conventional generators that can be employed for power grid dynamic stability. However, it is necessary to keep an energy buffer [20].

As the fuel input for a BG-based Genset can be regulated, a biogas Genset (BG) and diesel Genset may be utilized as the controlled generating unit for a low power network, such as an SPVS and WECS. In the last decade, urban electrification has advanced dramatically. Electrification has occurred in developing countries, but uninterrupted power supply remains a problem. These areas have been without power for some time. The primary causes of disrupted power supply are insufficient grid supplies, reliance on conventional generation, long-length transmission, and the value of urban and industrial parts [21,22]. The authors presented numerous microgrid methods based on a review of the literature. However, it was not reasonable to donate an interconnected self-sufficient city with power availability relying on load segregation and setting the priority loads. To ensure an uninterrupted power supply, a stability enhancement for interconnected microgrids has been proposed to observe network dynamics while transferring power among both microgrids.

The importance of reducing power loss in the production of electricity is being emphasized in another effort to reduce CO_2 emissions and the effects of global warming. As a result, there is little heat produced. The amount of heat that needs to be cooled is modest [23–25], so in theory energy conservation can further reduce the price and energy used by the cooling apparatus. To minimize online power loss, it is possible to determine the ideal reference voltage [26] and the best power flow [27,28] for each microgrid. An offline optimization approach [29] is offered to improve the load sheading machine's working point and reduce loss, but using an offline solution requires optimum operational conditions with little to no variable change. Meanwhile, power converter losses are given consideration.

In the AC microgrid, the converter loss may account for more than half of the total distribution loss [30]. Therefore, incorporating it into the control structures would significantly reduce the distribution power loss. In [31], a function of active and reactive power was almost perfectly suited to the entire distribution power loss of two connected AC microgrids. The active and reactive power of each generation unit was then divided using the optimization algorithm. The objective function of the power loss of each generator unit and the AC link between two areas was used to estimate the overall distribution power loss of two interconnected AC microgrids, which includes line loss and power loss of each region. In order to meet the need of the load according to the objective function, you

should also think about splitting power between two locations. Therefore, by offline adaptively modifying the controller's optimal settings, the minimization of the distribution loss can be achieved.

A distributed optimization approach for global distribution loss minimization is given with power sharing across generation units [32,33]. The findings of the simulation support the proposed control method for lowering the distribution power loss of two connected AC microgrids.

The final difficulty is enhancing the frequency of the microgrid under the conditions of the significant penetration of renewable energy sources. Installing low-inertia power generation units through fast-acting energy storage systems (ESS) with virtual inertia controllers, which have been the subject of much recent research [34–41], is one approach. Every control method has advantages and limitations of its own. The microgrid system's position enables ideal energy management. To maximize power flow inside the setup, a local energy management system may control generators (and presumably also loads). Depending on the kind of operation, several objectives are set for energy management: grid-connected or an island [42]. The typical goals in the grid-connected mode are to reduce the price of the energy import at the PCC, advance the power factor at the PCC, and optimize the voltage profile through the microgrid [43]. The primary objectives of power management in the islanded mode, as described in [43], are system improvement and the encouragement of a high frequency and voltage flexibility. We concentrated on a virtual inertia control method intended to reduce frequency deviation issues in islanded AC interconnected microgrids as opposed to the following thorough reviews, which concentrated on the implementation of virtual inertia topologies [41], virtual inertia and frequency control for distributed energy generation units [44], and inertia valuation improvement in power systems [45]. In particular, we sought to explain why specific control methods are more effective under various circumstances and which control methods will receive greater attention in the coming years. Finally, we suggest some analyses for the AC interconnected microgrid applications' use of the virtual inertia control approach. In this paper, five controllers, i.e., a proportional integral controller (PI), a fractional order PI controller (FOPI), a fuzzy PI controller (FPI), a fuzzy fractional order PI controller (FFOPI), and a VIC based on FFOPI, are used for controlling the frequency, voltage, and optimal power management of two interconnected microgrids. The optimal parameters of the controllers were optimized using particle swarm optimization (PSO). The objective function was considered to be the multi-objective function of integral time square error (ITSE) of the frequency, voltage, and the total distributed power loss of the two AC interconnected microgrids. This model was developed based on realistic city generation availability and was tested in a typical scenario.

Despite the rich literature review, and much research dealing with power quality enhancement in interconnected microgrids, the contributions of this paper are manifold. (a) The novelty of this modelling, in contrast to [22], is demonstrated to achieve the sharing of the active and reactive power of both generation units and between both microgrids through a tie line to guarantee the conception of an uninterrupted power supply. (b) The novelty of this work, in addition to [22,26,28], is demonstrated to achieve optimal power management for two areas' interconnected hybrid microgrid systems by using a multi-objective function equation for minimizing voltage deviation, frequency deviation, and the total distribution power loss of the AC interconnected microgrid. (c) In addition to [38], the proposed ESS based on virtual inertia control is a grid-forming element that can operate with an RES without requiring conventional energy sources. As a result, it improves the supply reliability during grid forming unit outages and solves the frequency regulation problem in islanded AC interconnected microgrids. (d) In addition to [46,47], under step load disturbances, step changes in wind/solar input power, and severe disturbances such as eventual grid following/forming contingencies, the improvement of the system performance using a PI, FOPI, FPI, FFOPID, and VIC based on FFOPI controllers for mitigating frequency and voltage oscillation and achieving optimal power

management in two AC interconnected microgrids with a multi objective function is investigated. (e) The PSO technique is utilized to automatically optimize the controller parameters while considering the system nonlinearity, converters and line dynamics, and the interaction components. This technique helps to reduce design work and costs. Additionally, any other optimization technique may be employed in future work to be compared with the PSO technique. This paper is organized as follows: In Section 2, the system under study and the mathematical modelling of the individual components system is explained. A study of the stability and power quality enhancement problems are discussed, and the utilized multi-objective function is stated, in Section 3. FPI and FFOPI block diagrams, membership functions, and rules are presented in Section 4, and virtual inertia control is proposed in Section 5. The optimization technique PSO is used in the optimization of five controller parameters in Section 6. The results and discussions are given in Section 7. Finally, Section 8 provides an overview of the provided work's conclusions. The appendix contains the system parameters, a list of symbols, and a list of abbreviations.

2. System under Study and Mathematical Modelling of the Two Interconnected Microgrids Component

The connected system is modelled under the presumption that microgrid M_1 has 50 kW of excess power that is sent to microgrid M_2. Under any circumstance, a steady-state variation in the power delivered over the interconnection occurs. Changes in demand or generation are handled locally by the microgrid systems. Figure 1 is a single line diagram (SLD) that shows the interconnected microgrid system.
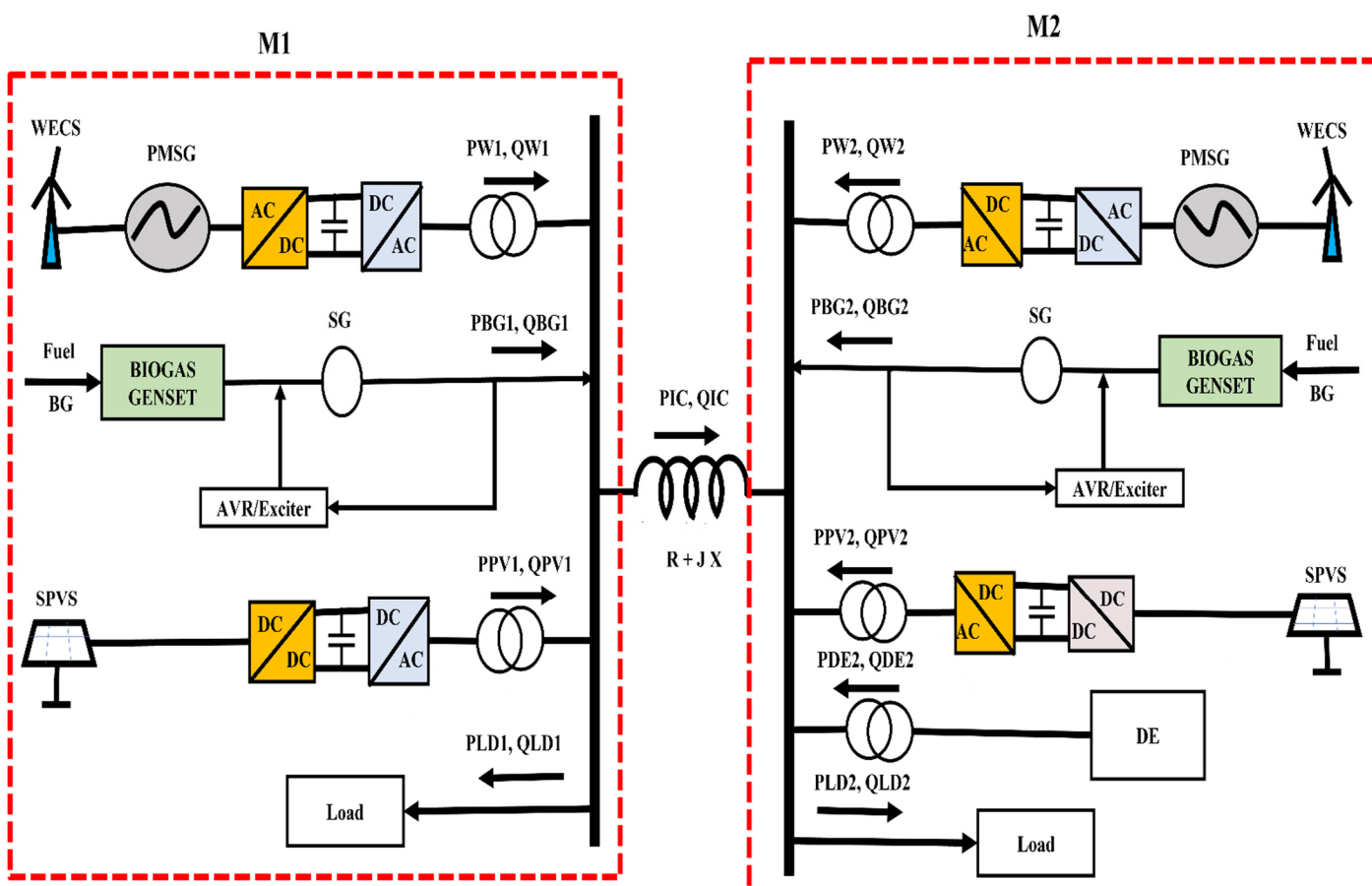

Figure 1. SLD of interconnected microgrid system.

Equations (1) and (2) can be used to express the real and reactive power balance at a steady state.

$$P_{LD} = P_W + P_{DE} + P_{PV} + P_{BG} \pm P_{IC} \tag{1}$$

$$Q_{LD} = Q_W + Q_{DE} + Q_{PV} + Q_{BG} \pm Q_{IC} \tag{2}$$

Equations (1) and (2) can be expressed as follows for a minor disturbance in power flows:

$$\Delta P_{LD} = \Delta P_W + \Delta P_{DE} + \Delta P_{PV} + \Delta P_{BG} \pm \Delta P_{IC} \tag{3}$$

$$\Delta Q_{LD} = \Delta Q_W + \Delta Q_{DE} + \Delta Q_{PV} + \Delta Q_{BG} \pm \Delta Q_{IC} \tag{4}$$

Real power demand and generation changes would affect the system's frequency, which in the Laplace domain can be expressed as follows:

$$\Delta F(S) = \frac{K_{FS}}{1 + s * T_{FS}} (\Delta P_W + \Delta P_{DE} + \Delta P_{PV} + \Delta P_{BG} \pm \Delta P_{IC} - \Delta P_{LD}) \tag{5}$$

The system bus voltage changes as a result of a change in the reactive power mismatch, as shown by:

$$\Delta V(S) = \frac{K_{VS}}{1 + s * T_{VS}} (\Delta Q_W + \Delta Q_{DE} + \Delta Q_{PV} + \Delta Q_{BG} \pm \Delta Q_{IC} - \Delta Q_{LD}) \tag{6}$$

2.1. Modelling of WECS with PMSG

A wind turbine with a permanent magnet synchronous generator that is connected to the common bus by a transformer and an AC/DC/AC power electronic interface was considered as a WECS. An easy line diagram is displayed in Figure 2. The real and reactive power flow equations are described by [22].

$$P_W = \frac{(V_{inW})(V)(sin\,(\theta_{inW} + \theta))}{X_{TWS}} \tag{7}$$

$$Q_W = \frac{((V_{inW})(V)(cos\,(\theta_{inW} + \theta))) - (V^2)}{X_{TWS}} \tag{8}$$

In the Laplace domain, a slight disturbance in power flows can be expressed as:

$$\Delta P_W^{'}(S) = K_{W1}\Delta V_{inW}(S) + K_{w2}\Delta V(S) + K_{w3}\Delta P_{inW} + K_{w4}\Delta\theta_{inw}(S) \tag{9}$$

$$\Delta Q_W^{'}(S) = K_{W5}\Delta V_{inW}(S) + K_{w6}\Delta V(S) + K_{w7}\Delta P_{inW} + K_{w8}\Delta\theta_{inw}(S) \tag{10}$$

where,

$$K_{W1} = \frac{\partial P_W}{\partial V_{inW}}, \;\; K_{W2} = \frac{\partial P_W}{\partial V}, \;\; K_{W3} = \frac{\partial P_W}{\partial p_{inw}}, \;\; K_{W4} = \frac{\partial P_W}{\partial \theta_{inw}}$$

$$K_{W5} = \frac{\partial Q_W}{\partial V_{inW}}, \;\; K_{W6} = \frac{\partial Q_W}{\partial V}, \;\; K_{W7} = \frac{\partial Q_W}{\partial p_{inw}} \;\; and \;\; K_{W8} = \frac{\partial Q_W}{\partial \theta_{inw}}$$

The system's inertia is credited with the delay as:

$$\Delta P_W(S) = \frac{1}{1 + S * T_W} \Delta P_W^{'}(S) \tag{11}$$

$$\Delta Q_W(S) = \frac{1}{1 + S * T_{W1}} \Delta Q_W^{'}(S) \tag{12}$$

The block diagram of the WECS can be created using Equations (9)–(12), as shown in Figure 3.
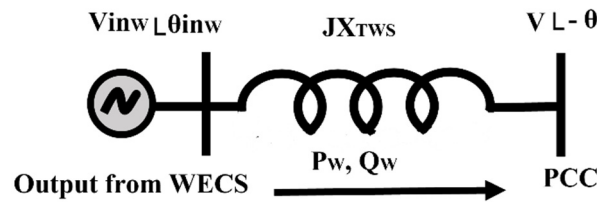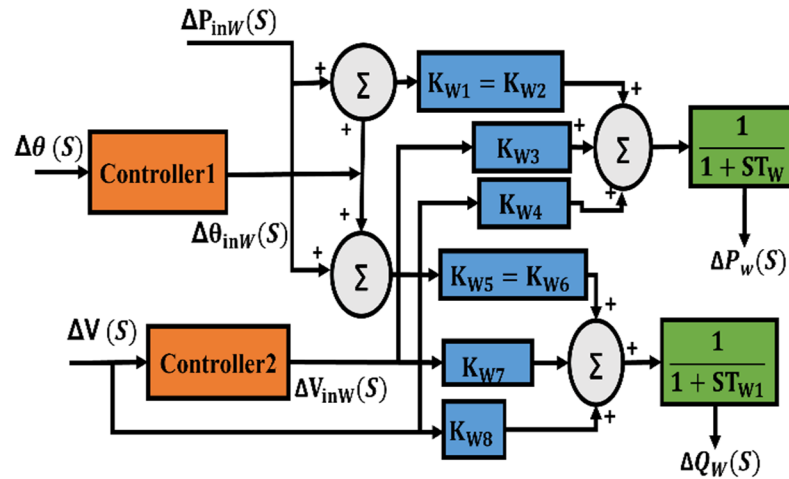
Figure 2. SLD of WECS.

Figure 3. The block diagram of WECS.

2.2. Modelling of a Solar PV System with an Inverter (SPVS)

A PV panel generates direct current as its form of power. Therefore, power is routed through a DC/DC/AC power electronic interface before connecting to the common bus, and it is then connected to the bus by a transformer. In Figure 4, the SLD figure is displayed, as in the case of the WECS. The following are the power flow equations that take into account internal reactance (X$_{TPV}$) are described by [22]:

$$P_{PV} = \frac{(V_{inPV})(V)(sin\,(\theta_{inPV} + \theta))}{X_{TPVS}} \tag{13}$$

$$Q_{PV} = \frac{((V_{inPV})(V)(cos\,(\theta_{inPV} + \theta))) - (V^2)}{X_{TPVS}} \tag{14}$$

$$\Delta P_{PV}^{'}\,(S) = K_{PV1}\Delta V_{inPV}\,(S) + K_{PV2}\Delta V(S) + K_{PV3}\Delta p_{inPV}(s) + K_{PV4}\Delta\theta_{inPV}(S) \tag{15}$$

$$\Delta Q_{PV}^{'}\,(S) = K_{PV5}\Delta V_{inPV}\,(S) + K_{PV6}\Delta V(S) + K_{PV7}\Delta p_{inPV}(s) + K_{PV8}\Delta\theta_{inPV}(S) \tag{16}$$

where

$K_{PV1} = \frac{\partial P_{PV}}{\partial V_{inPV}}, K_{PV2} = \frac{\partial P_{PV}}{\partial V}, K_{PV3} = \frac{\partial P_{PV}}{\partial P_{inPV}}, \; K_{PV4} = \frac{\partial P_{PV}}{\partial \theta_{inPV}}, \; K_{PV5} = \frac{\partial Q_{PV}}{\partial V_{inPV}}, K_{PV6} = \frac{\partial Q_{PV}}{\partial V}, \; K_{PV7} = \frac{\partial PQ_{PV}}{\partial P_{inPV}}, \text{ and } K_{PV8} = \frac{\partial Q_{PV}}{\partial \theta_{inPV}}$

The delay due to inertia of the system is accounted as:

$$\Delta P_{PV}(S) = \frac{1}{1 + S * T_{PV}} \; \Delta P_{PV}^{'}\,(S) \tag{17}$$

$$\Delta Q_{PV}(S) = \frac{1}{1 + S * T_{PV}} \; \Delta Q_{PV}^{'}\,(S) \tag{18}$$

Using Equations (15)–(18), the transfer function block diagram of SPVS can be constructed as shown in Figure 5.
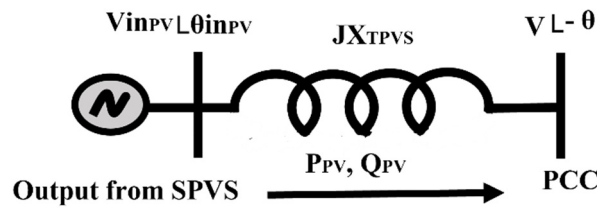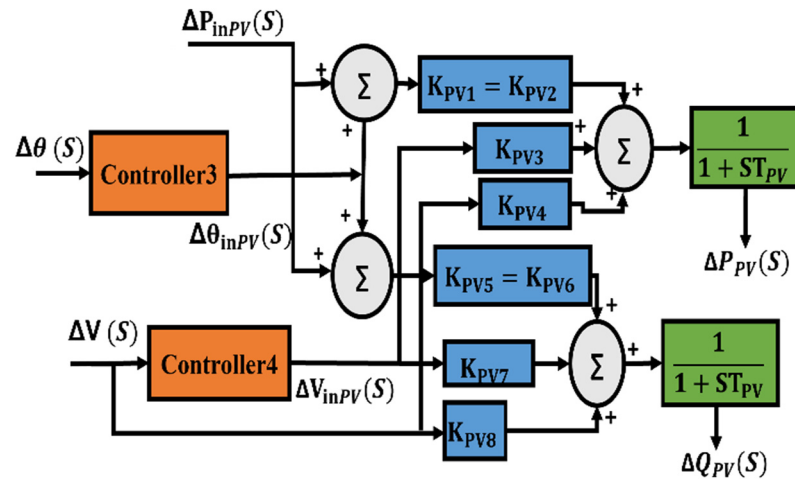
Figure 4. SLD of SPVS.

Figure 5. The block diagram of SPVS.

2.3. Modelling of BG

The BG model is based on [22]. Figure 6a,b demonstrate the transfer function block diagrams of a real power generation model and a reactive power generation model.
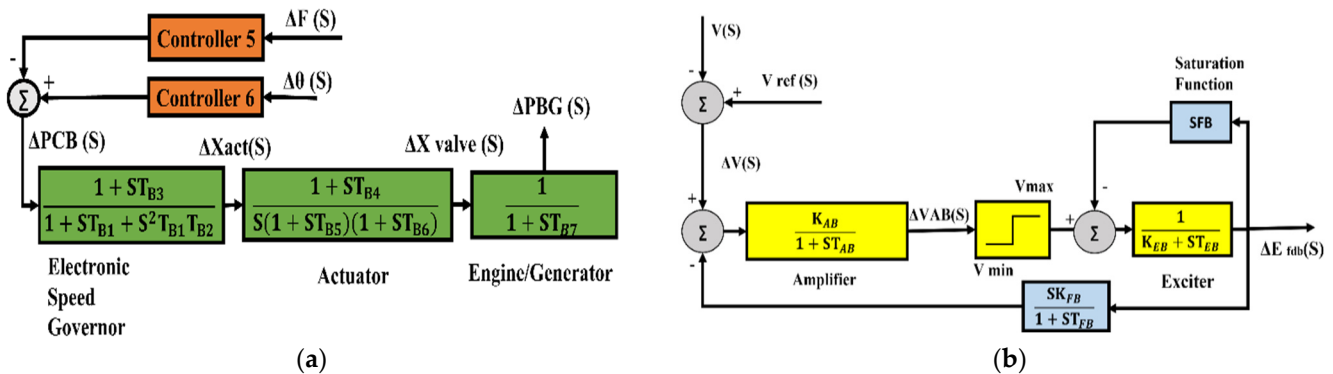

Figure 6. (**a**) Block diagram of real power generation of biogas and (**b**) block diagram of reactive power generation of biogas.

The voltage regulation operation of the AVR (automatic voltage regulator) and exciter is responsible for controlling reactive power in biogas (Figure 6). The equations for real and reactive powers are obtained and provided by considering the dynamic state after disregarding the saturation function:

$$\Delta E'_{qB}(S) = \frac{1}{1 + S * T_B}\left[K_{1B}\Delta E_{fdB}(S) + K_{2B}\Delta V(S)\right] \tag{19}$$

$$\Delta Q_B(S) = K_{3B}\Delta E'_{qB}(S) + K_{4B}\Delta V(S) \tag{20}$$

where

$$T_B = \frac{T'_{do} X'_d}{X_d}, K_{1B} = \frac{X'_d}{X_d}, \ K_{2B} = \frac{\left(X_d - X'_d\right)\cos(\delta+\theta)}{X_d}, \ K_{3B} = \frac{V\cos(\delta+\theta)}{X'_d} \ \text{and} \ K_{4B} = \frac{E'_{qB}\cos(\delta+\theta)-2V}{X'_d}$$

2.4. Modelling of DE

In a power-controlled DE system, the energy delivered daily is left unchanged but with a lowered, consistent, and continuous power supply. This keeps the power given by the diesel engine constant during the time period.

$$P_{DE} = \frac{E_{DE} V_2 sin(\theta_2)}{X_{DE}} \tag{21}$$

$$Q_{DE} = \frac{E_{DE} V_2 cos(\theta_2) - V_2^2}{X_{DE}} \tag{22}$$

Following a perturbation, Equations (21) and (22) can be written as:

$$\Delta P_{DE}(S) = K_{1DE}\Delta\theta_2(S) + K_{2DE}\Delta V_2(S) \tag{23}$$

$$\Delta Q_{DE}(S) = K_{3DE}\Delta\theta_2(S) + K_{4DE}\Delta V_2(S) \tag{24}$$

where

$$K_{1DE} = \frac{\partial P_{DE}}{\partial\theta}, \ K_{2DE} = \frac{\partial P_{DE}}{\partial V}, \ K_{3DE} = \frac{\partial Q_{DE}}{\partial\theta}, \text{and} \ K_{4DE} = \frac{\partial Q_{DE}}{\partial V}$$

2.5. Modelling of AC Interconnection

The interconnection was modelled taking into account an AC short transmission line. The line cannot be regarded as lossless because of its high R/X ratio. Figure 7 displays the AC line's transfer function block diagram. Such a line's source of power flow is:

$$P_{IC} = \frac{V_1 V_2}{Z} cos(\theta_z - \emptyset_{12}) - \frac{V_2^2}{Z^2} R_a \tag{25}$$

$$Q_{IC} = \frac{V_1 V_2}{Z} sin(\theta_z - \emptyset_{12}) - \frac{V_2^2}{Z^2} X \tag{26}$$

where θ_Z is the line's angle between R_a and X and ϕ_{12} is the difference between the voltage angles of bus 1 and bus 2. The Laplace domain Equations (25) and (26) have the following form for a minor perturbation:
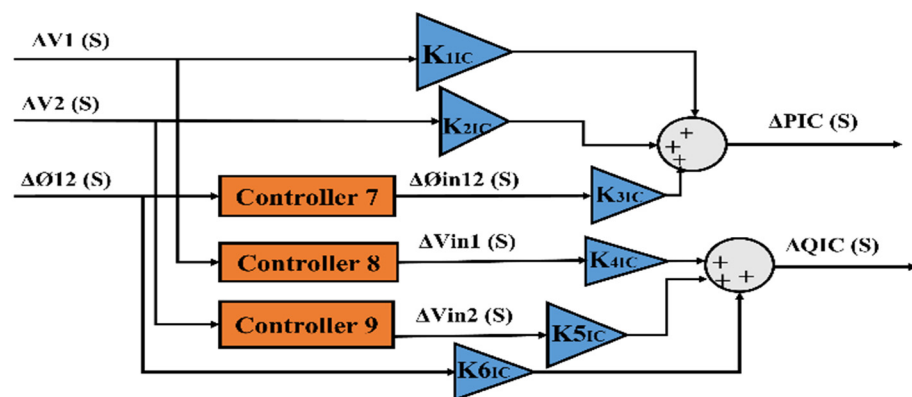

Figure 7. Transfer function block diagram of AC line.

$$\Delta P_{IC}(S) = K_{1IC}\Delta V_1(S) + K_{2IC}\Delta V_2(S) + K_{3IC}\Delta\emptyset_{in12}(S) \tag{27}$$

$$\Delta Q_{IC}(S) = K_{4IC}\Delta V_{in1}(S) + K_{5IC}\Delta V_{in2}(S) + K_{6IC}\Delta \emptyset_{12}(S) \tag{28}$$

where

$$K_{1IC} = \frac{\partial P_{IC}}{\partial V_1}, K_{2IC} = \frac{\partial P_{IC}}{\partial V_2}, K_{3IC} = \frac{\partial P_{IC}}{\partial \emptyset_{12}}, K_{4IC} = \frac{\partial Q_{IC}}{\partial V_1}, \ K_{5IC} = \frac{\partial Q_{IC}}{\partial V_2}, \text{ and } \ K_{6IC} = \frac{\partial Q_{IC}}{\partial \emptyset_{12}}$$

The microgrids were modelled using the above individual models of generation units. The data for microgrid M_2 was taken from [22,23] and the data for M_1 arose from slightly changing the data for M_2. Four medium-sized villages, each of which is anticipated to use roughly 1600 kW of electricity, are served by M_2, which was created to satisfy their demands. M_2 has a maximum diversity demand of 1000 kW. (approx.). The power supply has a frequency of 50 Hz and a rated voltage of 1 pu. The M_1 model was created for a group of both tiny and medium sized settlements. M_1 has a nominal generating capacity of 1150 kW and a maximum demand capacity of 700 kW, 50 Hz, and a rated voltage of 1 pu. Table 1 shows the steady state generation characteristics of the two microgrids. In total, 50 kW of continuous power are transmitted through an AC link from the M_1 microgrid to the M_2 microgrid, and, after losses, 40.6 kW are delivered to the M_2 microgrid. Table 2 provides a summary of the total power consumption, the power transfer from the AC link, and the generation from all the generating units in M_1 and M_2.

Table 1. Steady-state generation values for both microgrids.

Sources	Real Power (kW)		Rated Capacity (kW)	
	M_1	M_2	M_1	M_2
DE	0	300	0	350
BG	350	309.4	550	550
WECS	200	200	400	400
SPVS	150	150	200	200
Total	700	959.4	1150	1500

Table 2. Energy balance at a steady state in both microgrids.

	M_1	M_2
Local load (kW)	1000	650
Total generation (kW)	959.4	700
AC Interconnection (kW)	40.6	−50

The novelty of this modelling, in contrast to [22,23], is demonstrated to achieve the sharing of active and reactive power together for the wind and solar generation units s well as between both microgrids to guarantee the conception of an uninterrupted power supply through a continuous generation–demand balance.

3. Fuzzy PI (FPI) and Fuzzy Fractional Order PI (FFOPI) For Interconnected Microgrids

The FPI controller has three coefficients, with these three being the normalized gains K_1, K_2, and K_3, as shown in Figure 8a, whereas the FFOPI controller has four coefficients, with three of them being the normalized gains K_1, K_2, and K_3 and one being a fractional order control system λ, as shown in Figure 8b. The FPI and FFOPI have two inputs named error E and rate of change of error CE and one output. PSO was used to make offline tuning for the three parameters for the FPI and four parameters for the FFOPI of each controller on the six controllers that are associated with each microgrid and the three controllers responsible for tie lines between them. There are fifteen controllers in the two AC interconnected microgrids. PSO was used to search the optimized parameters of the FPI and FFOPI controllers to minimize the objective function according to the following equation:

$$J = \int_0^\infty t.\left(|\Delta F_1^2(t)| + |\Delta F_2^2(t)| + |\Delta V_1^2(t)| + |\Delta V_2^2(t)| + \left|\Delta S_{loss}^{total^2}(t)\right|\right)dt \tag{29}$$

The fuzzy logic (FLC) rules are listed as follows in Table 3. Figure 9 show the membership of output and input, where N = negative, p = positive, SP = small positive, Z = zero, SN = small negative, LP = large positive, and LN = large negative [47]. Any crisp value is defined in two fuzzy sets thanks to the uniform distribution of the input sets, which are triangle and cross neighbor sets with a membership value of 0.5. For ease of defuzzification, the output membership functions are assumed to be uniformly distributed singletons.

The first phase in the design method was to transfer the PI and FOPI gains to the linear fuzzy controller by replacing the known PI and FOPI with a linear FPI and linear FFOPI. According to the feed-back error signal $e(n)$, the traditional PI controller and FOPI controller signal $u(n)$ at any given time instant n can be stated either in absolute form, as in Equations (30) and (31), or incremental form, as in Equations (32)–(34).

$$u(n) = K_p\, e(n) + K_I\, \Sigma_{i=1}^n e(n)T_s \tag{30}$$

$$u(n) = K_p\, e(n) + K_I^\lambda \Sigma_{i=1}^n e(n)T_s \tag{31}$$

$$\Delta u(n) = K_p\, \Delta e(n) + K_I\, T_s\, e(n) \tag{32}$$

$$\Delta u(n) = K_p\, \Delta e(n) + K_I^\lambda\, T_s\, e(n) \tag{33}$$

$$\Delta e(n) = e(n) - e(n-1) \tag{34}$$

where, T_s is the sampling period, K_p and K_I are the proportional and integral gains, respectively, and λ is the integral fractional order control system.

The most often used defuzzification technique uses the concept of the center of gravity and is expressed as follows:

$$u = \frac{\Sigma_{i=1}\, u(u_i)\, u_i}{\Sigma_i\, u(u_i)} \tag{35}$$

where $u(u_i)$ represents the element's membership grade or weight, which is the result of the rule i.
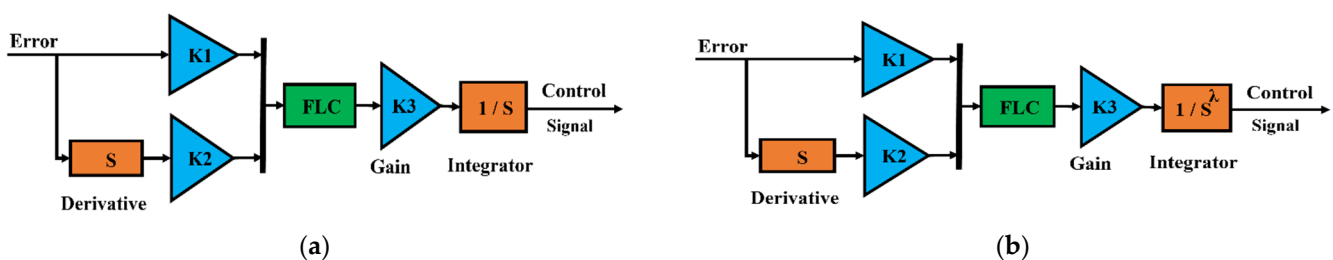

(**a**)

(**b**)

Figure 8. Block diagram of controller (**a**) Fuzzy PI and (**b**) Fuzzy fractional order PI.
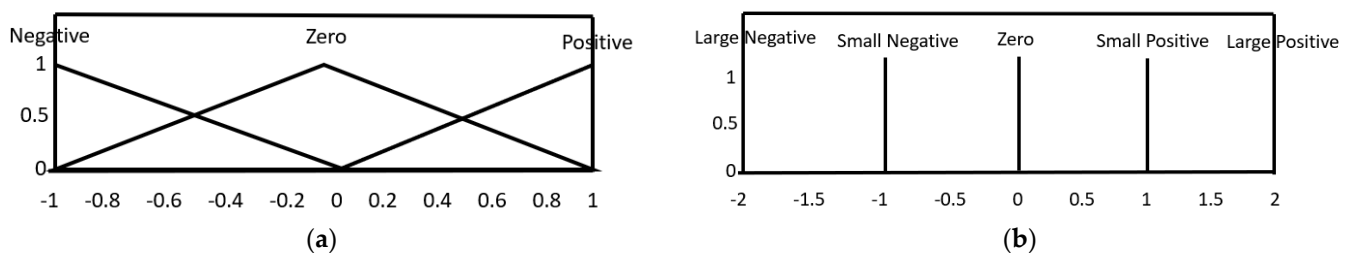

(**a**)

(**b**)

Figure 9. Membership for E and CE (**a**) input membership and (**b**) output membership.

Table 3. Fuzzy rule base.

E\CE	N	Z	P
N	LN	SN	Z
Z	S N	Z	S P
P	Z	S P	L N

4. Multi-Objective Function for Interconnected Microgrids

Numerical simulations were used to demonstrate the stability study (SS) in two interconnected systems for a disturbance, such as an increase in real and reactive power demand in both microgrids by each one, increased wind speed, solar radiation, and emergency/recovery from generation. The five controllers can reduce the step disturbance-induced steady-state error in frequency and voltage in the interconnected microgrids. The distribution power loss (DPL) in two interconnected microgrids is composed of eight parts: three parts for the first microgrid, which includes the power loss from the wind, PV, and biogas sources; four parts for the second microgrid, which includes the power loss from the wind, PV, biogas, and diesel engines; and one part for the AC interconnected line power loss. The average conduction losses of the PMSG, rectifier, inverter, and transformer are included in the wind power loss, whereas the average conduction losses of the DC-DC converter, inverter, and transformer are included in the PV power loss, the average conduction losses of the synchronous generator are included in the BG power loss, the average conduction losses of the diesel engine and transformer are included in the DE power loss, and the average conduction losses of the tie-line impedance are included in the line power loss. The distribution power loss of two interconnected microgrids is given by:

$$\Delta S_{loss}^{M1} = \Delta S_{loss}^{WECS1} + \Delta S_{loss}^{PV1} + \Delta S_{loss}^{BG1} \tag{36}$$

$$\Delta S_{loss}^{M2} = \Delta S_{loss}^{WECS2} + \Delta S_{loss}^{PV2} + \Delta S_{loss}^{BG2} + \Delta S_{loss}^{DE2} \tag{37}$$

$$\Delta S_{loss}^{total} = \Delta S_{loss}^{M1} + \Delta S_{loss}^{M2} + \Delta S_{loss}^{line} \tag{38}$$

where

$$\Delta S_{loss}^{WECS1} = \frac{\Delta V_1^2}{X_{TWS1}}, \ \Delta S_{loss}^{WECS2} = \frac{\Delta V_2^2}{X_{TWS2}}, \Delta S_{loss}^{PVS1} = \frac{\Delta V_1^2}{X_{TPV1}}, \ \Delta S_{loss}^{PVS2} = \frac{\Delta V_2^2}{X_{TPV2}},$$

$$\Delta S_{loss}^{BG1} = \frac{\Delta V_1^2}{X_{d1}'}, \Delta S_{loss}^{BG2} = \frac{\Delta V_2^2}{X_{d2}'}, \ \Delta S_{loss}^{DE2} = \frac{\Delta V_2^2}{X_{DE}}, \ \text{and} \ \Delta S_{loss}^{line} = \frac{\Delta V_2^2}{Z^2} R_a + \frac{\Delta V_2^2}{Z^2} X$$

To guarantee power quality enhancement, the OF must include two terms. The first term will achieve stability study by minimizing the OF based on ITSE criteria for the voltage and frequency of two interconnected microgrids. The second term will achieve optimal power flow by minimizing the OF based on ITSE criteria for the DPL of two interconnected microgrids. The five controllers' parameters are tuned using the PSO algorithm for minimizing the OF based on ITSE criteria for the voltage, frequency, and distribution power loss of two interconnected microgrids, as shown in Equation (39), and the tuned values are listed in Tables 4–6.

$$J = \int_0^\infty t. \left(|\Delta F_1^2(t)| + |\Delta F_2^2(t)| + |\Delta V_1^2(t)| + |\Delta V_2^2(t)| + \left| \Delta S_{loss}^{total^2}(t) \right| \right) dt \tag{39}$$

Table 4. Controller gains of microgrid system M₁ for PI, FOPI, FPI, and FFOPI controllers.

Controllers	PI Controller		FOPI Controller			FPI Controller			FFOPI Controller			
Parameters	KP	KI	KP	KI	λ	K1	K2	K3	K1	K2	K3	λ
Controller1	0.2	1	0.2	1	1	76.92	0.3947	0.013	76.92	0.3947	0.013	0.99
Controller2	−40	−8.4	−50	−18.4	0.99	5555.6	0.0139	0.0663	5555.6	0.0051	0.1923	0.98
Controller3	0.2	1	0.2	1	1	76.92	0.3947	0.013	76.92	0.3947	0.013	0.999
Controller4	−140	−3	−150	−3	0.965	5555.6	0.0111	0.0635	5555.6	0.0046	0.1895	0.9653
Controller5	6.04	2.36	6.04	2.36	0.98	76.92	0.0127	0.0307	76.92	0.0127	0.0307	1
Controller6	−3.15	−25.60	−3.15	−25.60	0.999	500	0.1591	0.0512	500	0.1591	0.0512	1

**Table 5.** Controller gains of microgrid system M₂ for PI, FOPI, FPI, and FFOPI controllers.

Controllers	PI Controller		FOPI Controller			FPI Controller			FFOPI Controller			
Parameters	KP	KI	KP	KI	λ	K1	K2	K3	K1	K2	K3	λ
Controller1	0.2	1	0.2	1	1	76.92	0.3947	0.013	76.92	0.3947	0.013	0.98
Controller2	−340	−5	−350	−15	0.98	76.92	1.09×10^{-4}	4.745	76.92	5.5×10^{-5}	13.85	0.889
Controller3	0.2	1	0.2	1	1	76.92	0.3947	0.013	76.92	0.3947	0.013	1
Controller4	240	−5	230	−15	0	76.92	0.0428	4.745	76.92	0.0078	13.85	0
Controller5	3.76	18.51	3.76	18.51	0.96	76.92	0.0205	0.2406	76.92	0.0205	0.2406	0.899
Controller6	−1.54	−32.68	−1.54	−32.68	0.978	333.3	0.2195	0.098	333.3	0.2195	0.098	1

Table 6. Controller gains of AC line for PI, FOPI, FPI, and FFOPI controllers.

Controllers	PI Controller		FOPI Controller			FPI Controller			FFOPI Controller			
Parameters	KP	KI	KP	KI	λ	K1	K2	K3	K1	K2	K3	λ
Controller7	0.2	1	0.2	1	1	76.92	0.3947	0.013	76.92	0.3947	0.013	1
Controller8	−40	−8.4	−50	−18.4	0.899	5555.6	0.0139	0.0663	5555.6	0.0051	0.1923	0.98
Controller9	−340	−5	−350	−15	0.897	76.92	1.09×10^{-4}	4.745	76.92	5.5×10^{-5}	13.85	0.9868

5. Virtual Inertia Control for Interconnected Microgrids

The substitute power for the real synchronous machine is provided by the virtual synchronous generator (VSG) [35,39]. In networks with a significant amount of renewable energy, this generator can be employed to increase the frequency stability. A particular VSG component known as a virtual inertia (VI) is used to make up for a lack of inertia via a power injection approach. Active frequency support is not possible due to the limitations of the virtual inertia mechanism. To handle nonlinearities in low-inertia systems, an extra robust controller is therefore required. The virtual inertia control structure (Figure 10) contains a derivative unit, a designed controller FFOPI, virtual inertia control (energy storage system and virtual inertia variable gain), and a power limiter ($\Delta P_{inertia,max}$, $\Delta P_{inertia,min}$).
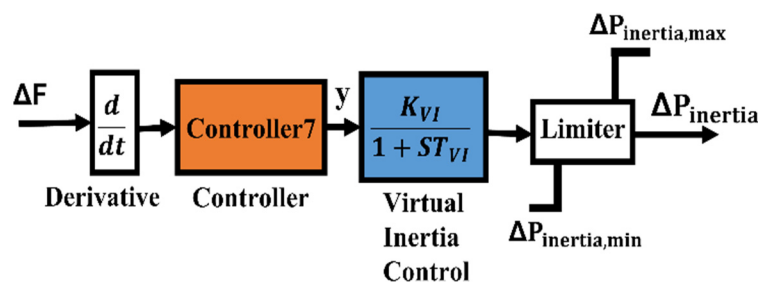
Figure 10. Typical structure of a virtual inertia control block.

The energy storage system (ESS), which may offer frequency smoothness and balance for subsequent dispatch, has emerged during the past ten years as a crucial component in renewable energy networks. The following characteristics of the ESS model are distinguishable:

$$G(S) = \frac{1}{T_{V1}S + 1} \tag{40}$$

Using the ITSE criteria, the FFOPI controller is set to minimize the OF. According to the ITSE requirements and as given in Equation (38), the PSO algorithm is used to optimize the FFOPI controller's parameters. Tables 7–9 include information on the FFOPI's tuned gain parameters. PSO also gives the values of K_{v1}, T_{v1}, which are 0.8 and 10, respectively.

Table 7. FFOPI controller gains of microgrid system M_1 in the case of VIC.

FFOPI	M_1			
Controller	K1	K2	K3	λ
FFOPI1	76.92	0.3947	0.013	0.99
FFOPI2	5555.6	0.0051	0.1923	0.98
FFOPI3	76.92	0.3947	0.013	0.999
FFOPI4	5555.6	0.0046	0.189	0.965
FFOPI5	76.92	0.0127	0.0307	1
FFOPI6	500	0.1591	0.0512	1
FFOPI7	50	0.005	0.2	0

Table 8. FFOPI controller gains of microgrid system M_2 in the case of VIC.

FFOPI	M_2			
Controller	K1	K2	K3	λ
FFOPI1	76.92	0.3947	0.013	0.98
FFOPI2	76.92	5.5×10^{-5}	13.85	0.889
FFOPI3	76.92	0.3947	0.013	1
FFOPI4	76.92	0.0078	13.85	0
FFOPI5	76.92	0.0205	0.2406	0.899
FFOPI6	333.3	0.2195	0.089	1
FFOPI7	50	0.005	0.2	0

Table 9. FFOPI controller gains of AC line in the case of VIC.

FFOPI	AC Line			
Controller	K1	K2	K3	λ
FFOPI8	76.92	0.3947	0.013	1
FFOPI9	5555.6	0.0051	0.1923	0.98
FFOPI10	76.92	5.5×10^{-5}	13.85	0.8968

6. Particle Swarm Optimization (PSO)

PSO replicates a swarm's collective activity when looking for food. The method is an iterative procedure that seeks to locate a solution within a search space that fulfils a fitness function [48]. The inherited composite nature, however, has been updated in various ways by PSO [46]. The PSO method is predicated on the idea that particles update their location and velocity after each iteration. As a result, with each iteration k, the current position X_i^k is modified in accordance with the particle's new velocity using the personnel best (PB) and the global best (GB), as shown in Equations (40) and (41), respectively.

$$X_i^k = X_i^{k-1} + V_i^k \tag{41}$$

$$V_i^k = w_0 . V_i^{k-1} + c_1 . r_1 . \left(GB - X_i^{k-1} \right) + c_2 . r_2 . (PB - X_i^{k-1}) \tag{42}$$

For the suggested PI, FOPI, FPI, FFOPI, and VIC based on FFOPI controllers, the PSO was employed in this study to improve controllers' parameters. Figure 11 depicts the PSO flow chart for the suggested application on the microgrid. Section 4 provides a thorough illustration of the objective function (j). The parameters for the optimization method are population = 50; iterations = 70; velocity clamping factor v = 2; cognitive C_1 = 2; social constant C_2 = 2; minimum inertial constant w_{min} = 0.4; maximum inertia constant w_{max} = 0.9. The PSO method has only been suggested for results analysis. Additionally, any other optimization technique may be employed without greatly affecting on the results.
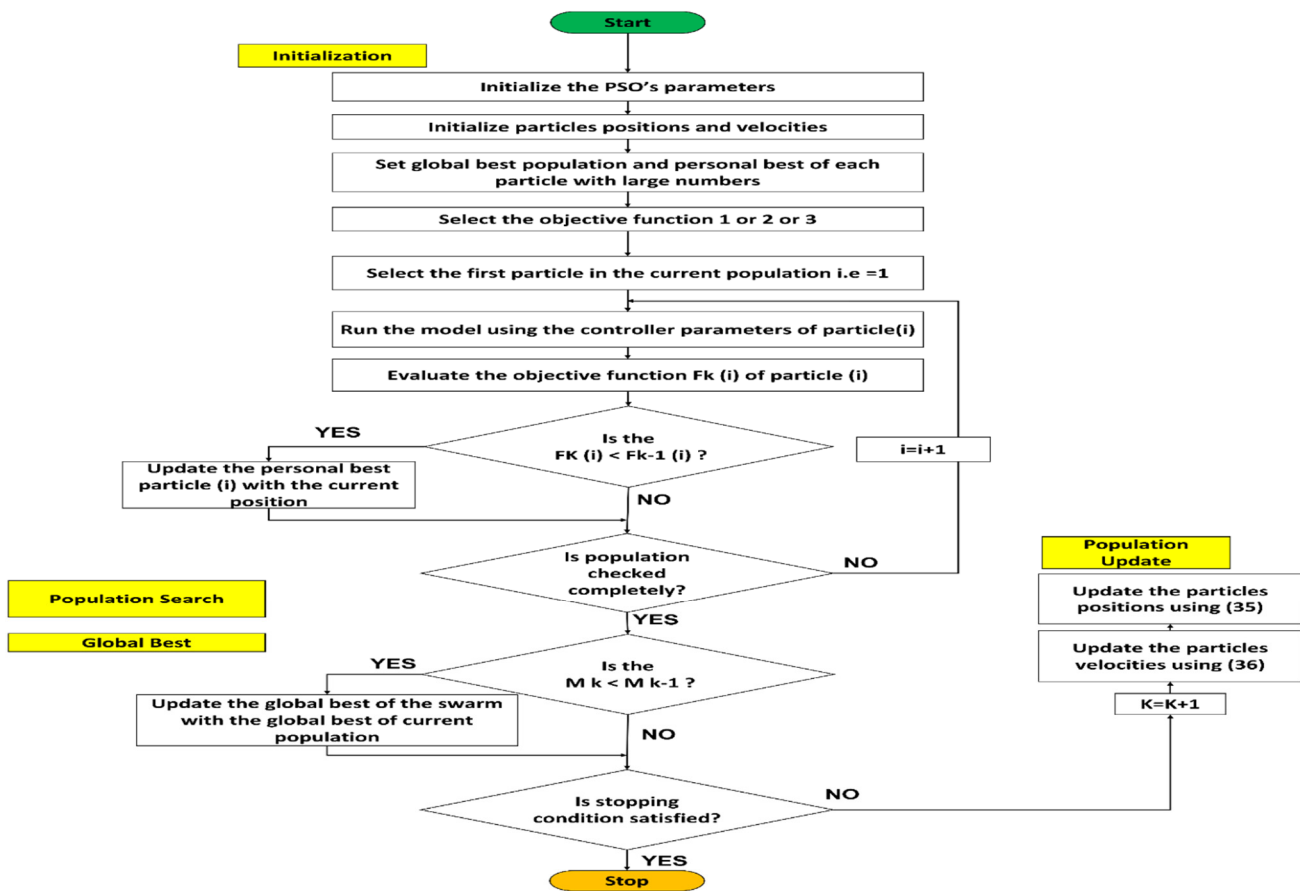

Figure 11. PSO algorithm flowchart.

7. Result and Discussion

The stability study, optimal power management, and virtual inertia control of the proposed interconnected two microgrids using five controllers based on PSO through a multi-objective function that were investigated by each controller include multiple disturbances. Each controller includes load disturbances, wind speed variation, solar radiation variation, and contingency/recovery of generation. The simulation results of the studied microgrid were carried out using MATLAB/Simulink software. The PI, FOPI, FPI, FFOPI and VIC based on FFOPI controllers using PSO through a multi-objective function will be discussed for each disturbance. The data of the system considered for simulation studies is given in the Appendix A.

7.1. Increasing Wind Speed with Load Variation Disturbance

The overall power generated on the microgrid increases as a result of the increased wind speed output power. This variance results in a power differential between the power that is generated and that which is needed, which may affect the microgrid's power management and frequency. In this scenario, the wind speed is suddenly increased by 1% in both microgrids at zero seconds while the load change demand is maintained at 0.01 pu. Without VIC, the inertia of the BG and the virtual inertia of the inverter coupled to the PVS and WECS balance out the energy imbalance. Contrarily, with VIC, the energy imbalance is balanced by the BG's inertia, the virtual inertia of the inverter connected to the PVS and WECS, and then the ESS of VIC, which supports the frequency during the period of disturbance until the BG's isochronous governor reacts to restore the steady-state frequency, thereby improving the frequency response. The change in the frequencies and voltages of microgrids M1 and M2 are shown in Figure 12.
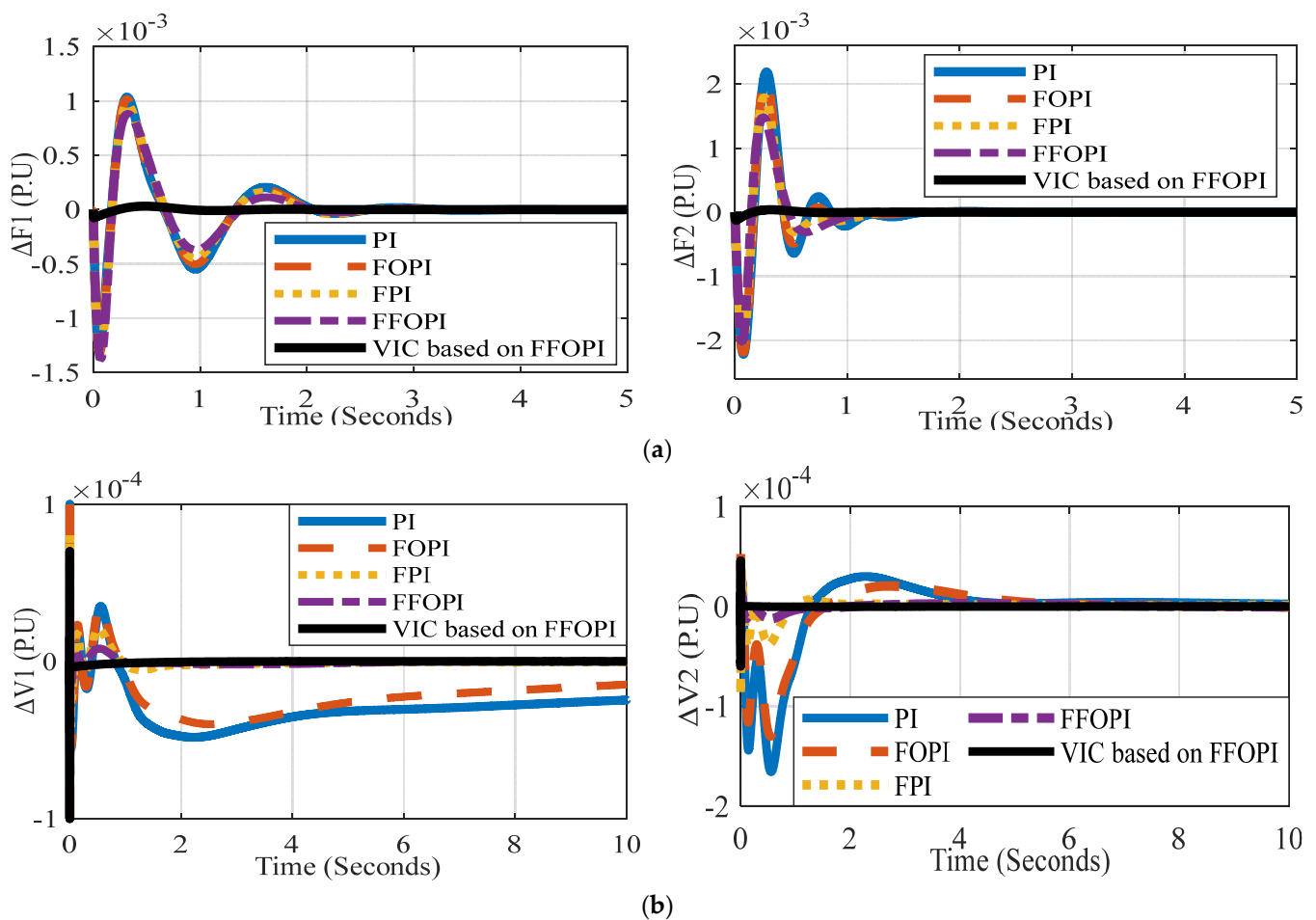
Figure 12. Interconnected microgrid's frequency and voltage measurements versus time for each controller at wind speed disturbance: (**a**) ΔF_1 (P.U), ΔF_2 (P.U), (**b**) ΔV_1 (P.U), ΔV_2 (P.U).

The dynamic specification (settling time (Ts), overshoot (Os), and undershoot (Us)) of frequencies and voltage deviation at each controller can be summarized in Table 10.

From Table 10, after the comparison of the five controllers, the VIC based on FFOPI minimizes overshoots Os and undershoots Us, improves system stability, and reduces the settling time Ts of the system for frequency deviation of both interconnected microgrids and, as a result, employs VIC based on FFOPI, which offers a superior response in terms of frequency enhancement compared to other controllers.

Table 10. Dynamic specification of frequencies and voltage deviation for each controller at wind speed disturbance.

Dynamic Deviation M1	PI	FOPI	FPI	FFOPI	VIC Based on FFOPI	Dynamic Deviation M2	PI	FOPI	FPI	FFOPI	VIC Based on FFOPI
ΔF1 Ts (S)	3.8	3.5	3.2	3	0.9	ΔF2 Ts (S)	2.5	2.2	1.9	1.5	0.5
Os (PU)	1.04×10^{-3}	1.02×10^{-3}	0.97×10^{-3}	0.88×10^{-3}	3.06×10^{-5}	Os (PU)	2.2×10^{-3}	2×10^{-3}	1.8×10^{-3}	1.5×10^{-3}	3.8×10^{-5}
Us (PU)	-1.2×10^{-3}	-1.3×10^{-3}	-1.33×10^{-3}	-1.4×10^{-3}	-7.5×10^{-5}	Us (PU)	-2×10^{-3}	-2.2×10^{-3}	-2×10^{-3}	-2×10^{-3}	-0.12×10^{-3}
ΔV1 Ts (S)	9	8.5	8	6.5	1	ΔV2 Ts (S)	9	7	5	4	0.015
Os (PU)	3.5×10^{-5}	3.55×10^{-5}	2×10^{-5}	8.3×10^{-6}	0	Os (PU)	3×10^{-5}	2.7×10^{-5}	2.4×10^{-5}	1.3×10^{-5}	4.7×10^{-7}
Us (PU)	-5.5×10^{-5}	-5.4×10^{-5}	-2.6×10^{-5}	-1.6×10^{-5}	-3.9×10^{-6}	Us (PU)	-0.16×10^{-3}	-0.13×10^{-3}	-4×10^{-5}	-1.3×10^{-5}	-2.7×10^{-7}

Table 11 demonstrates the power-sharing of each generating unit in two microgrids at each controller, balancing for the power differential during this disturbance through a multi-objective function which supports the minimum total power loss. The investigation of Figures 13 and 14 can be justified in Table 11. Due to the increase in wind speed disturbance, the new value of the change in the active power of the WECS for both microgrids, M1 and M2, equals (0.01 * Pw) added to the change in the active power of the WECS at step load change only without wind speed disturbance.
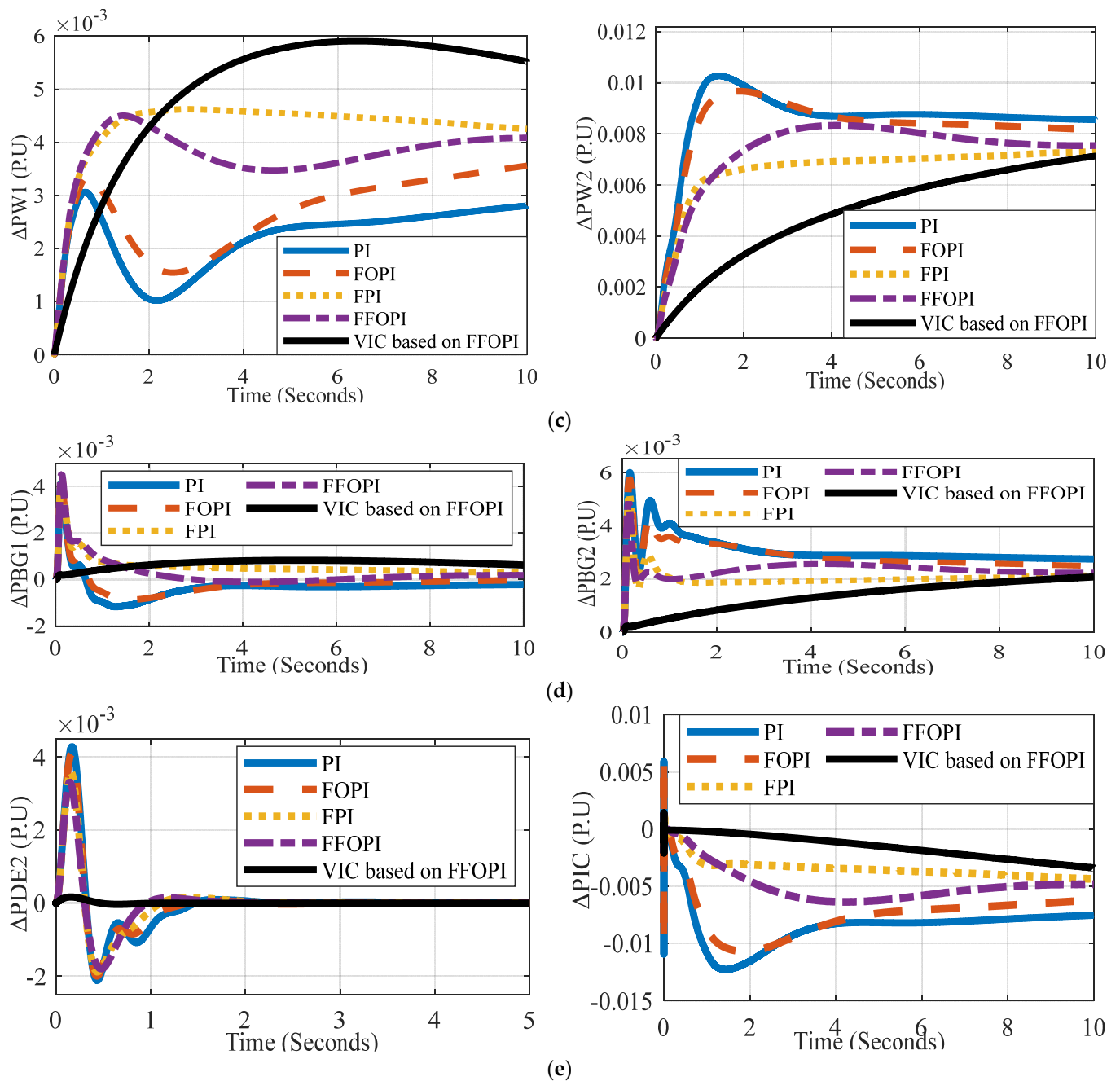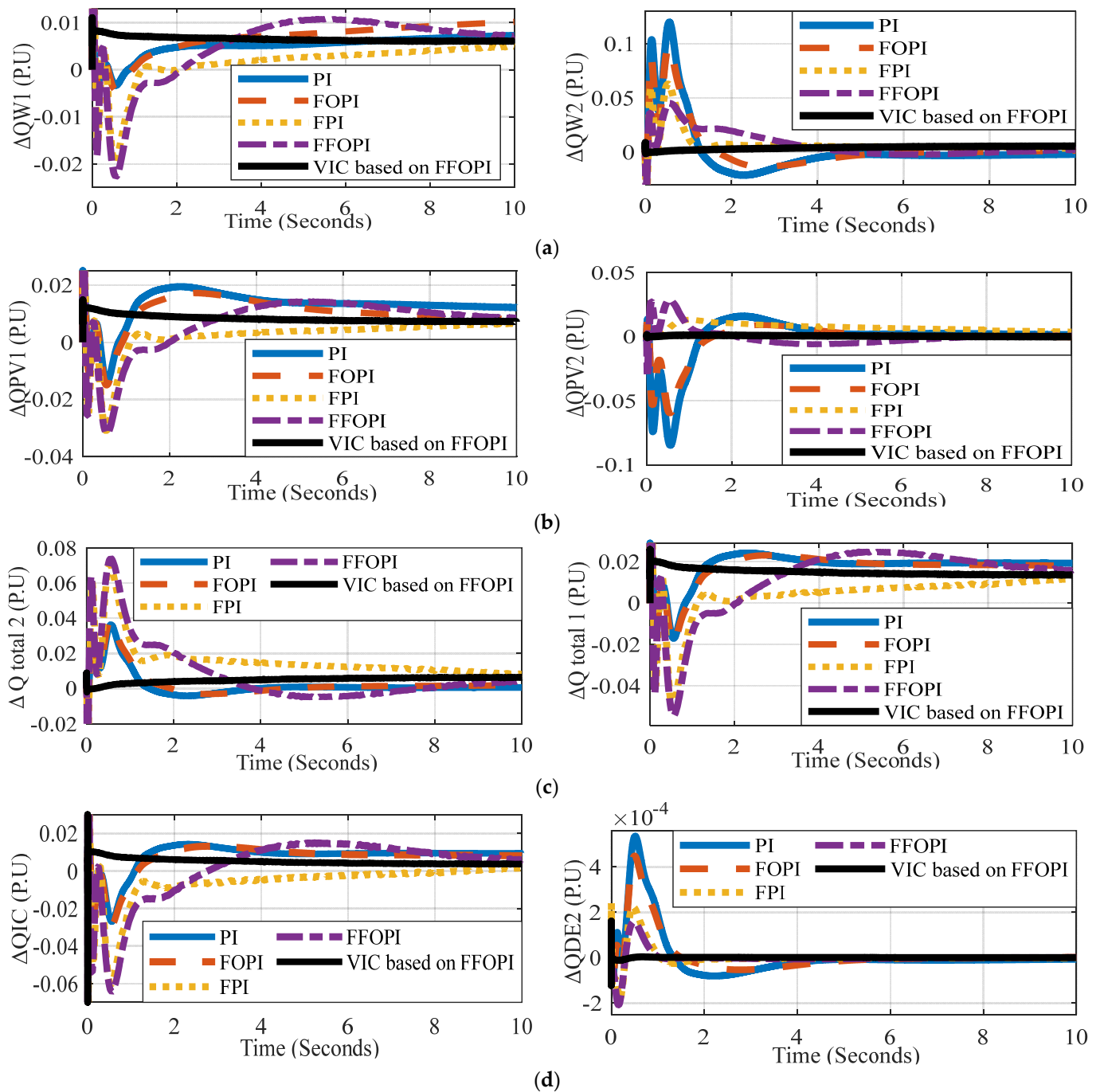

(a)

(b)

(c)

(d)

(e)
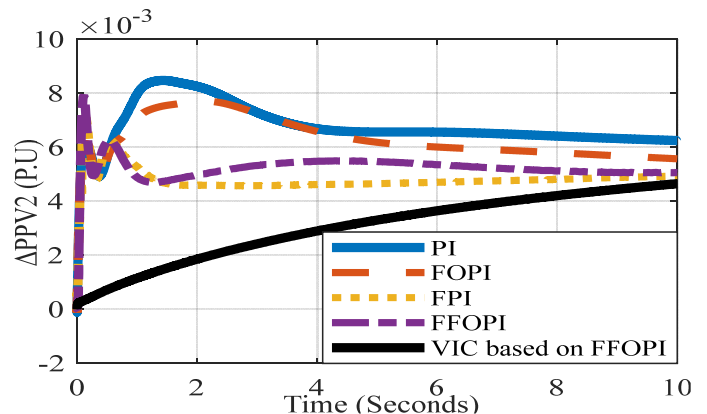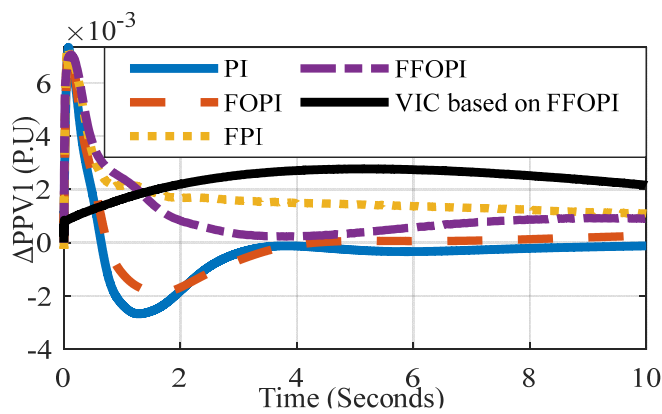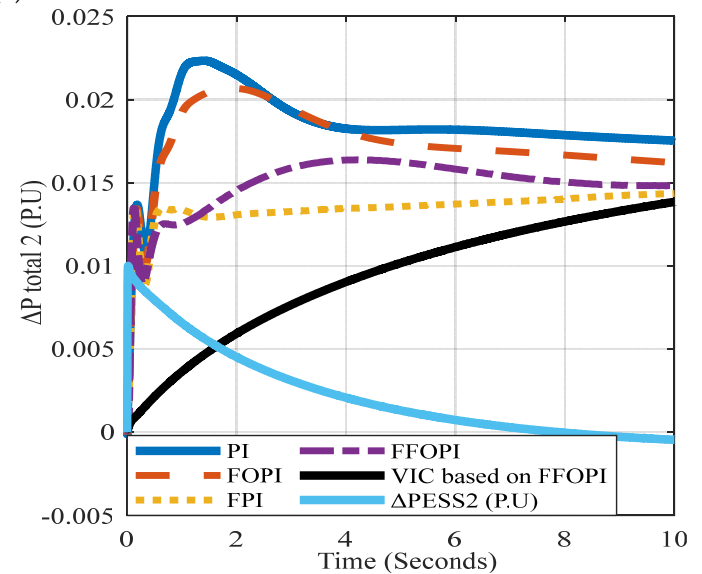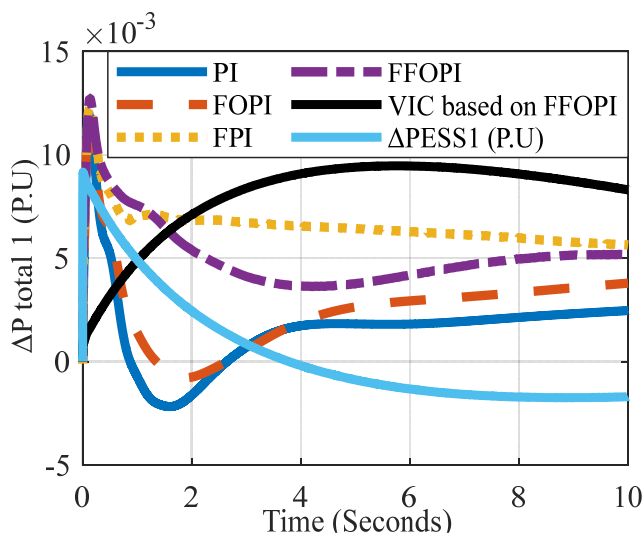
Figure 13. M_1 and M_2's active power measurements versus time for each controller at wind speed disturbance: (**a**) ΔP_{PV1} (PU), ΔP_{PV2} (PU), (**b**) $\Delta P_{total\,1}$ (PU), $\Delta P_{total\,2}$ (PU), (**c**) ΔP_{w1} (PU), ΔP_{w2} (PU), (**d**) ΔP_{BG1} (PU), ΔP_{BG2} (PU), (**e**) ΔP_{DE2} (PU), ΔP_{IC} (PU).

Table 11. Power flow in pu of microgrid system M_1 and M_2 for each controller at wind speed disturbance.

M_1 Power Deviation	PI	FOPI	FPI	FFOPI	VIC Based on FFOPI	M_2 Power Deviation	PI	FOPI	FPI	FFOPI	VIC Based on FFOPI
ΔP_{BG1}	-0.2×10^{-3}	-2.6×10^{-5}	0.3×10^{-3}	0.2×10^{-3}	0.6×10^{-3}	ΔP_{BG2}	2.7×10^{-3}	2.5×10^{-3}	2.1×10^{-3}	2.2×10^{-3}	2.1×10^{-3}
ΔP_{W1}	2.8×10^{-3}	3.6×10^{-3}	4.3×10^{-3}	4.1×10^{-3}	5.5×10^{-3}	ΔP_{W2}	8.5×10^{-3}	8.2×10^{-3}	7.3×10^{-3}	7.5×10^{-3}	7.1×10^{-3}
ΔP_{PV1}	-0.1×10^{-3}	0.3×10^{-3}	1×10^{-3}	0.9×10^{-3}	2.2×10^{-3}	ΔP_{PV2}	6.2×10^{-3}	5.6×10^{-3}	4.9×10^{-3}	5.1×10^{-3}	4.7×10^{-3}
ΔP_{ESS1}	-	-	-	-	-1.7×10^{-3}	ΔP_{ESS2}	-	-	-	-	-0.46×10^{-3}
ΔP_{IC12}	-7.5×10^{-3}	-6.2×10^{-3}	-4.4×10^{-3}	-4.8×10^{-3}	-3.4×10^{-3}	ΔP_{IC21}	7.5×10^{-3}	6.2×10^{-3}	4.4×10^{-3}	4.8×10^{-3}	3.4×10^{-3}
ΔP_{total1}	2.5×10^{-3}	3.8×10^{-3}	5.6×10^{-3}	5.2×10^{-3}	8.3×10^{-3}	ΔP_{total2}	17.4×10^{-3}	16.3×10^{-3}	14.3×10^{-3}	14.8×10^{-3}	13.9×10^{-3}
ΔQ_{W1}	7.3×10^{-3}	10.1×10^{-3}	4.9×10^{-3}	7.3×10^{-3}	6×10^{-3}	ΔQ_{W2}	-2×10^{-3}	1.3×10^{-3}	3.3×10^{-3}	2.1×10^{-3}	5.6×10^{-3}
ΔQ_{PV1}	12.1×10^{-3}	7.9×10^{-3}	6.5×10^{-3}	8.6×10^{-3}	7.2×10^{-3}	ΔQ_{PV2}	1.3×10^{-3}	-0.62×10^{-3}	3.9×10^{-3}	0.69×10^{-3}	-2.82×10^{-5}
ΔQ_{BG1}	-0.1×10^{-3}	0.1×10^{-3}	0.2×10^{-3}	0.1×10^{-3}	0.3×10^{-3}	ΔQ_{BG2}	1.37×10^{-3}	1.22×10^{-3}	1.2×10^{-3}	1.21×10^{-3}	0.93×10^{-3}

| ΔQ_{IC12} | 9.3×10^{-3} | 8.1×10^{-3} | 1.6×10^{-3} | 6×10^{-3} | 3.5×10^{-3} | ΔQ_{IC21} | -9.3×10^{-3} | -8.1×10^{-3} | -1.6×10^{-3} | -6×10^{-3} | -3.5×10^{-3} |
| ΔQ_{total1} | 19.3×10^{-3} | 18.1×10^{-3} | 11.6×10^{-3} | 16×10^{-3} | 13.5×10^{-3} | ΔQ_{total2} | 0.67×10^{-3} | 1.9×10^{-3} | 8.4×10^{-3} | 4×10^{-3} | 6.5×10^{-3} |

Figure 14. M_1 and M_2's reactive power measurements versus time for each controller at wind speed disturbance: (**a**) ΔQ_{w1} (PU), ΔQ_{W2} (PU), (**b**) ΔQ_{PV1} (PU), ΔQ_{PV2} (PU), (**c**) $\Delta Q_{\text{total 1}}$ (PU), $\Delta Q_{\text{total 2}}$ (PU), (**d**) ΔQ_{IC} (PU), ΔQ_{DE2} (PU).

As can be seen from Table 11, the ESS acts through VIC as a load to support the frequency. Equation (38) can be used to calculate the power loss of two interconnected microgrids, and the results are 7.6×10^{-9} for the PI controller, 2.7×10^{-9} for the FOPI, 1.96×10^{-11} for the FPI, 6.3×10^{-12} for the FFOPI, and 2.2×10^{-13} for the VIC based on FFOPI due to the minimum value of power sharing (ΔP_{IC} and ΔQ_{IC}) through the tie line at the VIC case. As a result, the best frequency performance and the optimal power flow are achieved in the case of the VIC based on FFOPI controller.

7.2. Increasing Solar Radiation with Load Variation Disturbance

The overall power generated on the microgrid increases due to an increase in solar radiation output power. With this variance, there is a power differential between the power that is generated and the power that is demanded, which may affect the microgrid's frequency and power management. In this scenario, the solar radiation is abruptly increased by 1% in both microgrids at zero seconds while the load fluctuation demand is maintained constant at 0.01 P.U.

Without VIC, the inertia of the BG and the virtual inertia of the inverter coupled to the PVS and WECS balance out the energy imbalance. While using VIC, the energy imbalance is balanced by the BG's inertia, the inverter's virtual inertia when connected to the PVS and WECS, and then the ESS of VIC, which supports the frequency during a disturbance period until the BG's isochronous governor reacts to recover the steady-state frequency. Figure 15 shows the change in frequencies and voltages of microgrids M1 and M2. The dynamic specification (Ts, Os, and Us) of frequencies and voltage deviation at each controller can be summarized in Table 12.

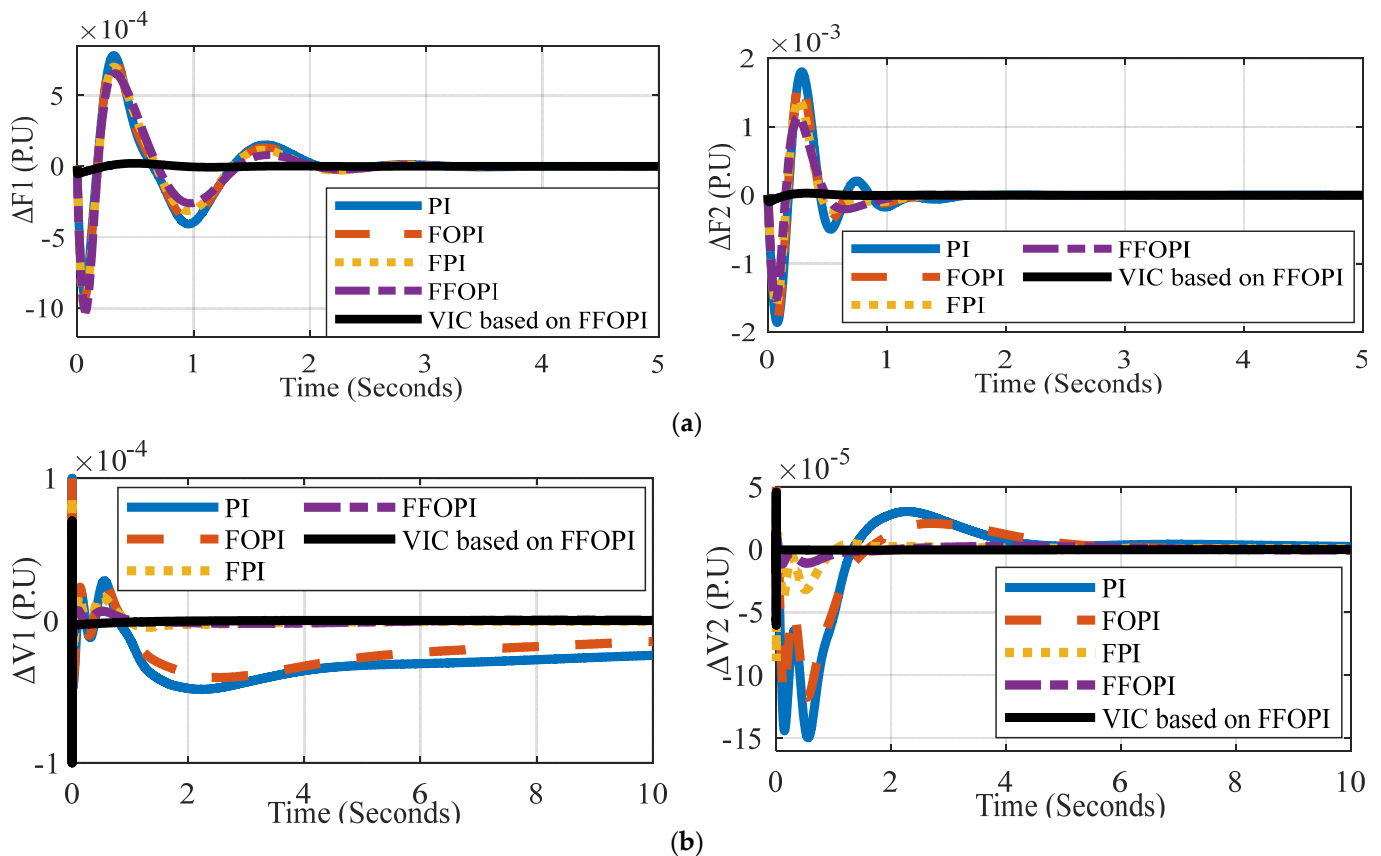**Figure 15.** Interconnected microgrid's frequency and voltage measurements versus time for each controller at solar radiation disturbance: (**a**) ΔF_1 (P.U), ΔF_2 (P.U), (**b**) ΔV_1 (P.U), ΔV_2 (P.U).

Table 12. Dynamic specification of frequencies and voltage deviation for each controller at solar radiation disturbance.

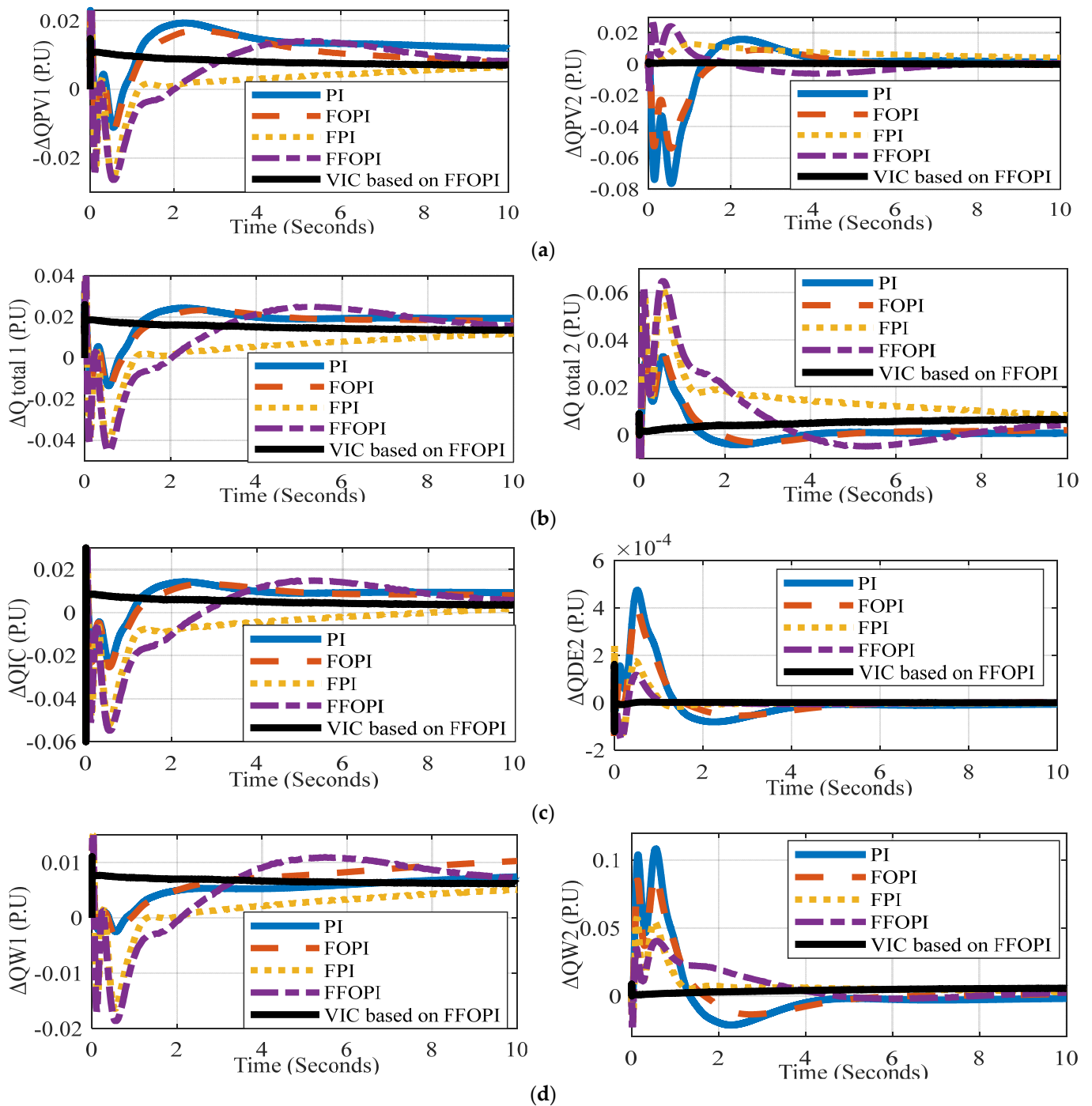| Dynamic Deviation M_1	PI	FOPI	FPI	FFOPI	VIC Based on FFOPI	Dynamic Deviation M_2	PI	FOPI	FPI	FFOPI	VIC Based on FFOPI
$\Delta F1$ Ts (S)	3.8	3.5	3.2	2.8	0.9	$\Delta F2$ Ts (S)	2.8	2.5	1.8	1.1	0.5
Os (PU)	0.9×10^{-3}	0.8×10^{-3}	0.7×10^{-3}	0.6×10^{-3}	2×10^{-5}	Os (PU)	1.8×10^{-3}	1.6×10^{-3}	1.3×10^{-3}	1.1×10^{-3}	2.9×10^{-5}
Us (PU)	-0.8×10^{-3}	-0.9×10^{-3}	-1×10^{-3}	-1.1×10^{-3}	-5.4×10^{-5}	Us (PU)	-1.8×10^{-3}	-1.7×10^{-3}	-1.6×10^{-3}	-1.5×10^{-3}	-9.6×10^{-5}
$\Delta V1$ Ts (S)	9	8	7	6.5	1	$\Delta V2$ Ts (S)	9	7	5	4	0.025
Os (PU)	2.8×10^{-5}	2.6×10^{-5}	1.6×10^{-5}	6.4×10^{-6}	0	Os (PU)	3×10^{-5}	2.1×10^{-5}	1.2×10^{-5}	7×10^{-6}	1.2×10^{-7}
Us (PU)	-4.8×10^{-5}	-4×10^{-5}	-1.7×10^{-5}	-1×10^{-5}	-3.5×10^{-6}	Us (PU)	-0.15×10^{-3}	-0.11×10^{-3}	-3.8×10^{-5}	-1.1×10^{-5}	-3×10^{-7}

As can be seen from Table 12 and a comparison of the five controllers, the VIC based on FFOPI provided the best response properties in terms of the Ts, Os, and Us of the system for both frequency deviations of the two interconnected microgrids. As a result, using VIC based on FFOPI offered a better response in terms of frequency enhancement when compared to the other controllers.

Table 13 show how the power-sharing of each generation unit in M_1 and M_2 at each controller compensate for the power imbalance during this disturbance through a multi-objective function to minimize the total power loss. The investigation of Figures 16 and 17 can be justified in Table 13. Due to the increase in solar radiation disturbance, the new value of the change in the active power of the SPVS for both microgrids M_1 and M_2 equals $(0.01 * P_{PV})$ added to the change in the active power of the SPVS at step load change only without solar radiation disturbance.

(a)

(b)
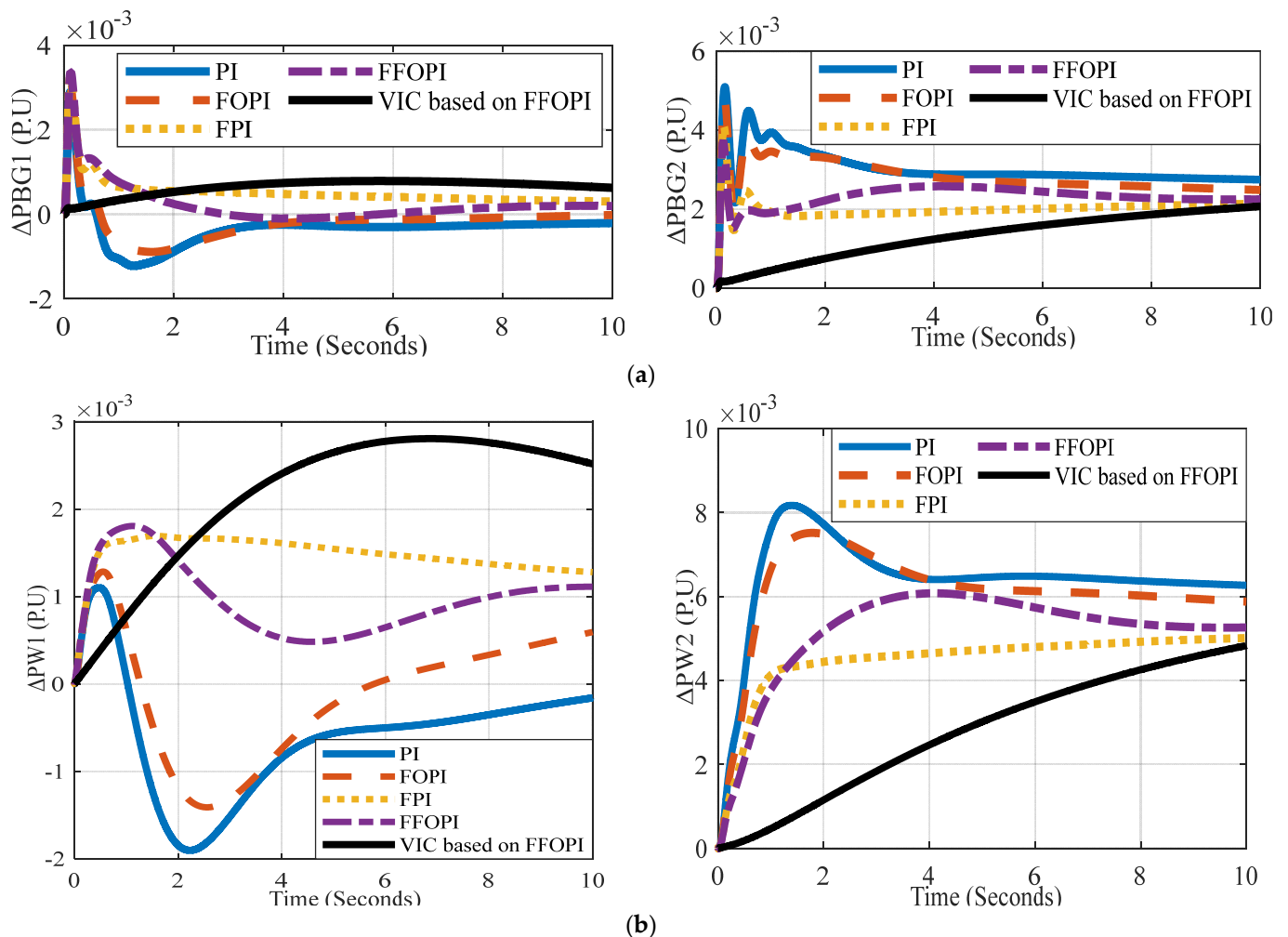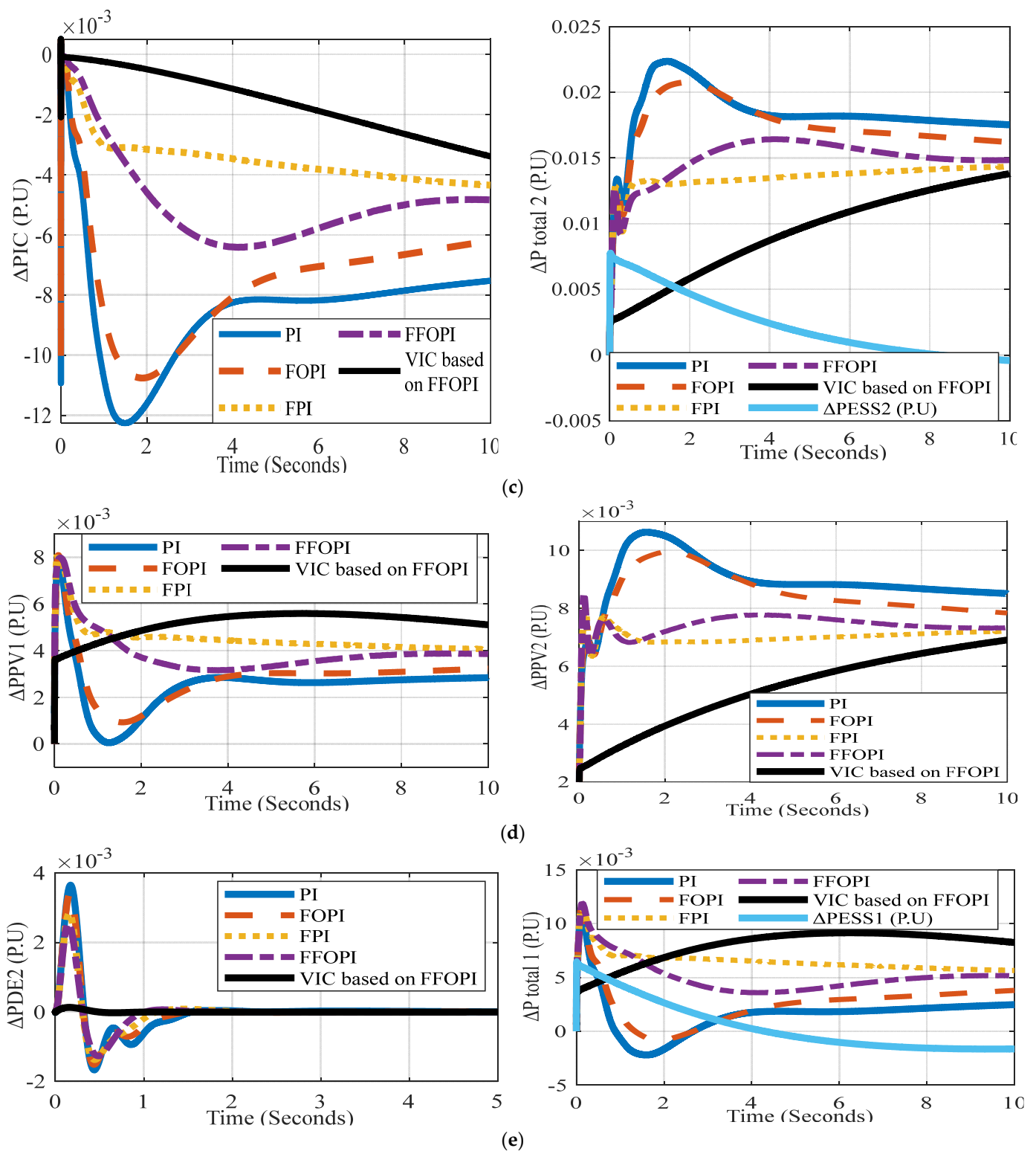
Figure 16. M$_1$ and M$_2$'s active power measurements versus time for each controller at solar radiation disturbance: (**a**) ΔP_{BG1} (PU), ΔP_{BG2} (PU), (**b**) ΔP_{W1} (PU), ΔP_{W2} (PU), (**c**) ΔP_{IC} (PU), $\Delta P_{total\ 2}$ (PU), (**d**) ΔP_{PV1} (PU), ΔP_{PV2} (PU), (**e**) ΔP_{DE2} (PU), $\Delta P_{total\ 1}$ (PU).

Figure 17. M_1 and M_2's reactive power measurements versus time for each controller at solar radiation disturbance: (**a**) ΔQ_{PV1} (PU), ΔQ_{PV2} (PU), (**b**) $\Delta Q_{\text{total 1}}$ (PU), $\Delta Q_{\text{total 2}}$ (PU), (**c**) ΔQ_{IC} (PU), ΔQ_{DE2} (PU), (**d**) ΔQ_{W1} (PU), ΔQ_{W2} (PU).

As can be seen from Table 13, the ESS acts through VIC as a load to support the frequency. The power loss of the two interconnected microgrids can be calculated using Equation (38), which resulted in 7.5×10^{-9} in the case of the PI controller, 2.7×10^{-9} in the case of the FOPI, 1.6×10^{-11} in the case of the FPI, 7.3×10^{-12} in the case of the FFOPI, and 7.1×10^{-14} in the case of the VIC based on FFOPI due to the minimum value of power sharing (ΔP_{IC} and ΔQ_{IC}) through the tie line at the VIC case. So, the VIC based on FFOPI controller provided a superior response with respect to frequency enhancement and optimal power managements compared to the other controllers.

Table 13. Power flow in pu of microgrid system M_1 and M_2 for each controller at solar radiation disturbance.

M_1 Power Deviation	PI	FOPI	FPI	FFOPI	VIC Based on FFOPI	M_2 Power Deviation	PI	FOPI	FPI	FFOPI	VIC Based on FFOPI
ΔP_{BG1}	-0.2×10^{-3}	-1.7×10^{-5}	0.3×10^{-3}	0.2×10^{-3}	0.63×10^{-3}	ΔP_{BG2}	2.7×10^{-3}	2.5×10^{-3}	2.1×10^{-3}	2.2×10^{-3}	2.1×10^{-3}
ΔP_{W1}	-0.2×10^{-3}	0.6×10^{-3}	1.3×10^{-3}	1.1×10^{-3}	2.5×10^{-3}	ΔP_{W2}	6.3×10^{-3}	5.9×10^{-3}	5.1×10^{-3}	5.3×10^{-3}	4.8×10^{-3}
ΔP_{PV1}	2.8×10^{-3}	3.2×10^{-3}	4.1×10^{-3}	3.8×10^{-3}	5.1×10^{-3}	ΔP_{PV2}	8.5×10^{-3}	7.8×10^{-3}	7.2×10^{-3}	7.3×10^{-3}	6.9×10^{-3}
ΔP_{ESS1}	-	-	-	-	-1.6×10^{-3}	ΔP_{ESS2}	-	-	-	-	-0.41×10^{-3}
ΔP_{IC12}	-7.5×10^{-3}	-6.2×10^{-3}	-4.4×10^{-3}	-4.8×10^{-3}	-3.4×10^{-3}	ΔP_{IC21}	7.5×10^{-3}	6.2×10^{-3}	4.4×10^{-3}	4.8×10^{-3}	3.4×10^{-3}
ΔP_{total1}	2.4×10^{-3}	3.8×10^{-3}	5.7×10^{-3}	5.1×10^{-3}	8.23×10^{-3}	ΔP_{total2}	17.5×10^{-3}	16.2×10^{-3}	14.4×10^{-3}	14.8×10^{-3}	13.8×10^{-3}
ΔQ_{W1}	7.4×10^{-3}	10.3×10^{-3}	5.1×10^{-3}	7.3×10^{-3}	6.3×10^{-3}	ΔQ_{W2}	-1.8×10^{-3}	1.5×10^{-3}	3.1×10^{-3}	2.5×10^{-3}	5.6×10^{-3}
ΔQ_{PV1}	12×10^{-3}	7.8×10^{-3}	6.4×10^{-3}	8.2×10^{-3}	7.1×10^{-3}	ΔQ_{PV2}	1.2×10^{-3}	-0.72×10^{-3}	4.1×10^{-3}	0.65×10^{-3}	-0.2×10^{-3}
ΔQ_{BG1}	-0.1×10^{-3}	-0.1×10^{-3}	0.2×10^{-3}	0.2×10^{-3}	0.3×10^{-3}	ΔQ_{BG2}	1.3×10^{-3}	1.22×10^{-3}	1.1×10^{-3}	1.15×10^{-3}	0.9×10^{-3}
ΔQ_{IC12}	9.3×10^{-3}	8×10^{-3}	1.7×10^{-3}	5.7×10^{-3}	3.7×10^{-3}	ΔQ_{IC21}	-9.3×10^{-3}	-8×10^{-3}	-1.7×10^{-3}	-5.7×10^{-3}	-3.7×10^{-3}
ΔQ_{total1}	19.3×10^{-3}	18×10^{-3}	11.7×10^{-3}	15.7×10^{-3}	13.7×10^{-3}	ΔQ_{total2}	0.7×10^{-3}	2×10^{-3}	8.3×10^{-3}	4.3×10^{-3}	6.3×10^{-3}

7.3. Contingency Event Disturbances Analysis

In this section, the microgrid was subjected to a large disturbance that resulted in a severe power imbalance, impacting on the frequency and power response as well as a brief outage of the tie line.

Case1: Disconnecting the Tie Line with Load Variation Disturbance

Other severe disturbances include the sudden outage of the tie line, which prevents power from transferring from one microgrid to another. Each microgrid is in charge of satisfying the demand load at its PCC. The tie line between two microgrids is activated at zero seconds in a sudden outage, while the load change demand is maintained at 0.01 pu throughout the simulation period. This variance results in a power differential between the power that is generated and that which is required, which may affect the microgrid's power management and frequency.

The inertia of the BG and the virtual inertia of the inverter instantly linked to the PVS and WECS of each microgrid correct for the frequency variation. However, employing the ESS could improve stability during a disturbance period until the BG's isochronous governor intervenes to restore the steady-state frequency. Figure 18 displays the variations in frequencies and voltages of microgrids M_1 and M_2. The dynamic specification of frequencies and voltage deviation at each controller can be summarized in Table 14.

Table 14. Dynamic specification of frequencies and voltage deviation for each controller at disconnecting tie line.

Dynamic Deviation M_1	PI	FOPI	FPI	FFOPI	VIC Based on FFOPI	Dynamic Deviation M_2	PI	FOPI	FPI	FFOPI	VIC Based on FFOPI
$\Delta F1$ Ts (S)	3.8	3.5	3.2	3	0.9	$\Delta F2$ Ts (S)	2.5	2.2	1.9	1.5	0.5
Os (PU)	9×10^{-3}	8.9×10^{-3}	8.8×10^{-3}	8.7×10^{-3}	3.1×10^{-5}	Os (PU)	3.6×10^{-3}	3.4×10^{-3}	1.7×10^{-3}	1.6×10^{-3}	3.7×10^{-5}
Us (PU)	-4×10^{-3}	-3.8×10^{-3}	-2×10^{-3}	-1.8×10^{-3}	-0.1×10^{-3}	Us (PU)	-3.9×10^{-3}	-3.8×10^{-3}	-2×10^{-3}	-1.8×10^{-3}	-0.12×10^{-3}
$\Delta V1$ Ts (S)	9	8.5	3	2	1.5	$\Delta V2$ Ts (S)	8	7	3	1	0.002
Os (PU)	0	0	0	0	0	Os (PU)	0	0	0	0	0
Us (PU)	-2.2×10^{-5}	-2×10^{-5}	-4.5×10^{-6}	-1.6×10^{-6}	-1.7×10^{-6}	Us (PU)	-1.4×10^{-3}	-1.3×10^{-3}	-7×10^{-6}	-3×10^{-6}	-2.8×10^{-6}
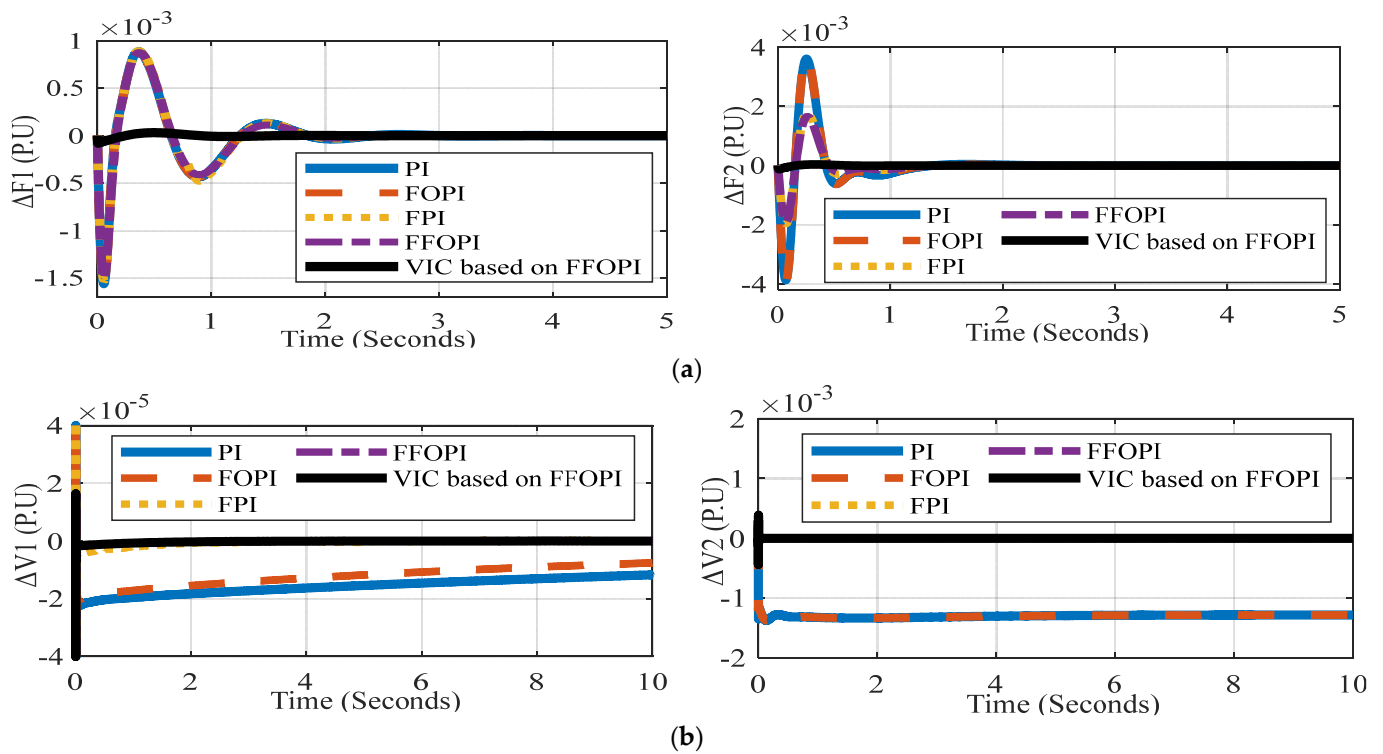
Figure 18. Interconnected microgrid's frequency and voltage measurements versus time for each controller at disconnected tie line disturbance: (**a**) ΔF_1 (P.U), ΔF_2 (P.U), (**b**) ΔV_1 (P.U), ΔV_2 (P.U).

As can be seen from Table 14 and a comparison of five controllers, the VIC based on FFOPI minimizes the Os and Us, improves system stability, and reduces the Ts of the system for both frequency deviations of the two interconnected microgrids; as a result, employing VIC offered a superior response in terms of frequency enhancement compared to the other controllers.

Table 15 illustrates the power-sharing of each generating unit in two microgrids at each controller balance for the power imbalance during this disturbance through a multi-objective function which supported the minimum total power loss. Table 15 facilitates the investigation of Figure 19.

Table 15. Power flow in pu of microgrid system M$_2$ and M$_2$ for each controller at disconnecting tie line.

| M$_1$ Power Deviation	PI	FOPI	FPI	FFOPI	VIC Based on FFOPI	M$_2$ Power Deviation	PI	FOPI	FPI	FFOPI	VIC Based on FFOPI
ΔP_{BG1}	1.4×10^{-3}	1.4×10^{-3}	1.3×10^{-3}	1.4×10^{-3}	1.6×10^{-3}	ΔP_{BG2}	1.3×10^{-3}	1.3×10^{-3}	1.7×10^{-3}	1.7×10^{-3}	2×10^{-3}
ΔP_{W1}	4.4×10^{-3}	4.4×10^{-3}	4.4×10^{-3}	4.4×10^{-3}	5×10^{-3}	ΔP_{W2}	15.2×10^{-3}	15.2×10^{-3}	4.2×10^{-3}	4.5×10^{-3}	5×10^{-3}
ΔP_{PV1}	4.2×10^{-3}	4.2×10^{-3}	4.3×10^{-3}	4.2×10^{-3}	5×10^{-3}	ΔP_{PV2}	-6.5×10^{-3}	-6.5×10^{-3}	4.1×10^{-3}	3.8×10^{-3}	4.6×10^{-3}
ΔP_{ESS1}	-	-	-	-	-1.6×10^{-3}	ΔP_{ESS2}	-	-	-	-	-1.6×10^{-3}
ΔP_{IC12}	0	0	0	0	0	ΔP_{IC21}	0	0	0	0	0
ΔP_{total1}	10×10^{-3}	10×10^{-3}	10×10^{-3}	10×10^{-3}	11.5×10^{-3}	ΔP_{total2}	10×10^{-3}	10×10^{-3}	10×10^{-3}	10×10^{-3}	11.6×10^{-3}
ΔQ_{W1}	3.6×10^{-3}	5.4×10^{-3}	4.1×10^{-3}	4.1×10^{-3}	4.2×10^{-3}	ΔQ_{W2}	4.6×10^{-3}	9.7×10^{-3}	4.6×10^{-3}	9.5×10^{-3}	9.2×10^{-3}
ΔQ_{PV1}	5.7×10^{-3}	4×10^{-3}	5.3×10^{-3}	4.9×10^{-3}	5×10^{-3}	ΔQ_{PV2}	4.6×10^{-3}	-0.6×10^{-3}	4.6×10^{-3}	-4.4×10^{-5}	0.2×10^{-3}
ΔQ_{BG1}	0.7×10^{-3}	0.6×10^{-3}	0.6×10^{-3}	1×10^{-3}	0.8×10^{-3}	ΔQ_{BG2}	0.8×10^{-3}	0.9×10^{-3}	0.8×10^{-3}	0.54×10^{-3}	0.6×10^{-3}
ΔQ_{IC12}	0	0	0	0	0	ΔQ_{IC21}	0	0	0	0	0
ΔQ_{total1}	10×10^{-3}	10×10^{-3}	10×10^{-3}	10×10^{-3}	10×10^{-3}	ΔQ_{total2}	10×10^{-3}	10×10^{-3}	10×10^{-3}	10×10^{-3}	10×10^{-3}

(a)

(b)

(c)

(d)

(**e**)

(**f**)

(**g**)

(**h**)
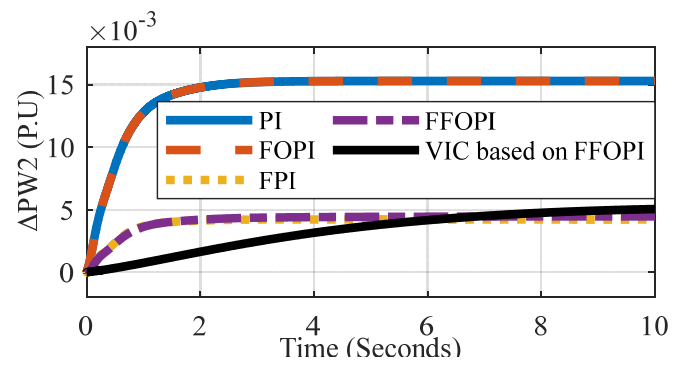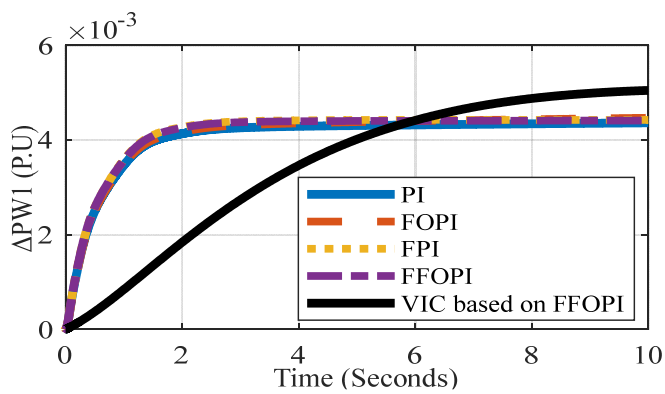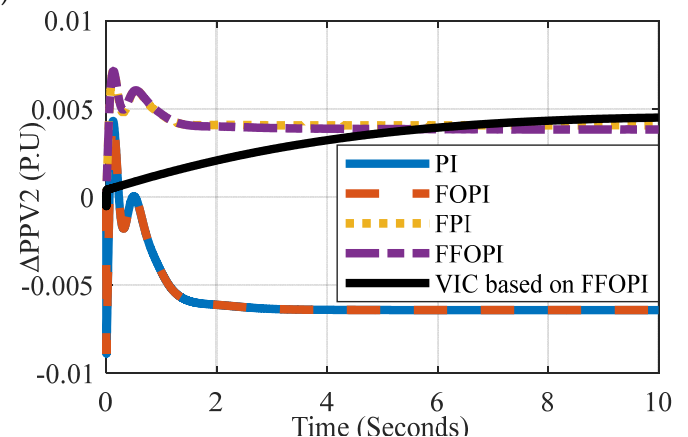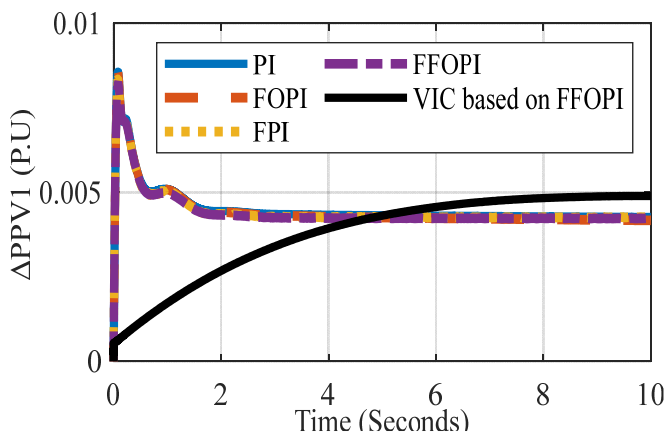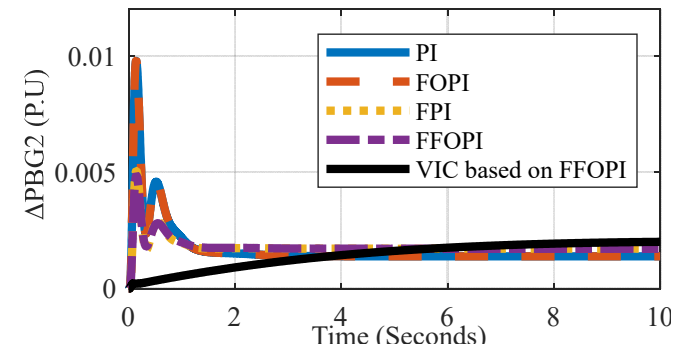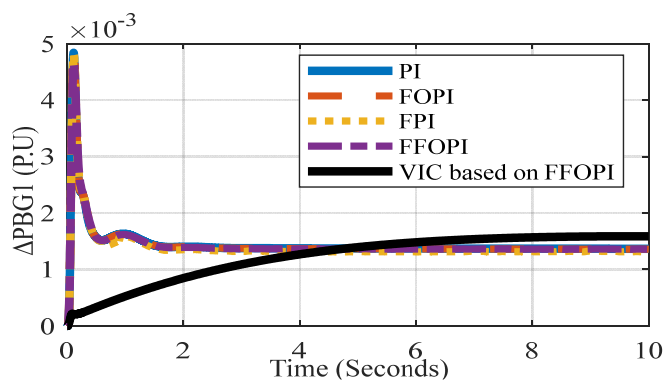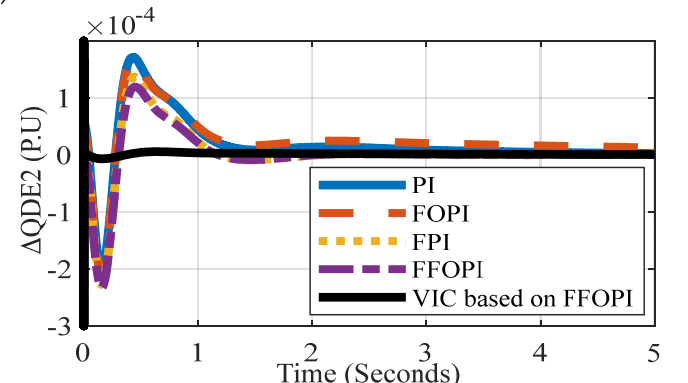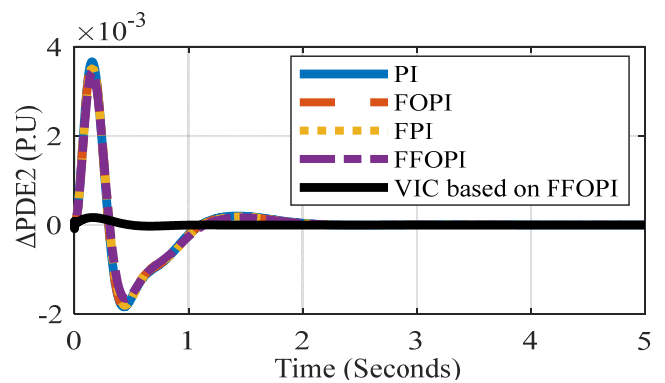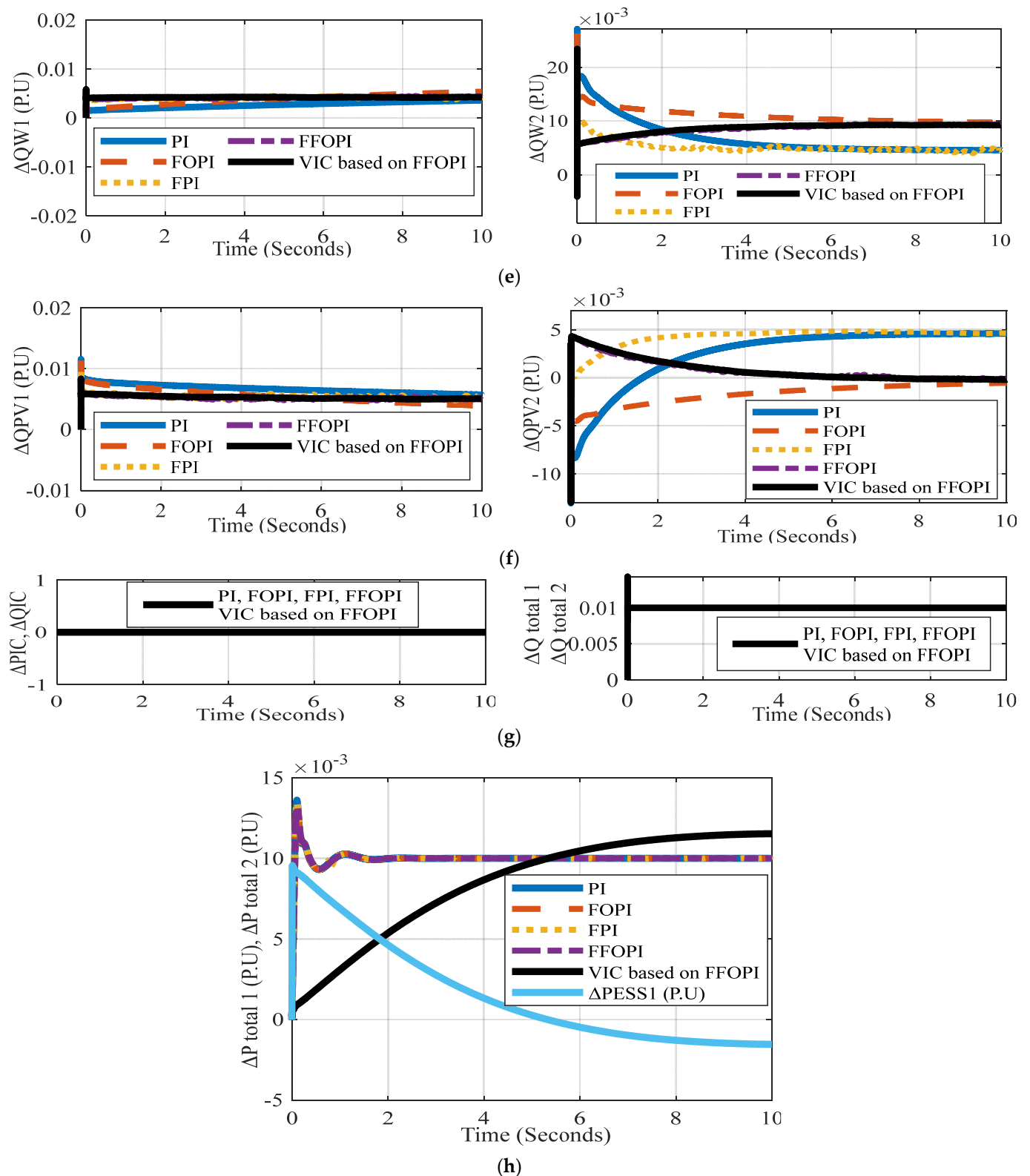
Figure 19. M₁ and M₂'s active and reactive power measurements versus time for each controller at disconnected tie line disturbance: (**a**) ΔP_{W1} (PU), ΔP_{W2} (PU), (**b**) ΔP_{PV1} (PU), ΔP_{PV2} (PU), (**c**) ΔP_{BG1} (PU), ΔP_{BG2} (PU), (**d**) ΔP_{DE2} (PU), ΔQ_{DE2} (PU), (**e**) ΔQ_{W1} (PU), ΔQ_{W2} (PU), (**f**) ΔQ_{PV1} (PU), ΔQ_{PV2} (PU), (**g**) ΔP_{IC} (PU), ΔQ_{IC} (PU), $\Delta Q_{\text{total 1}}$ (PU), $\Delta Q_{\text{total 2}}$ (PU), (**h**) $\Delta P_{\text{total 1}}$ (PU), $\Delta P_{\text{total 2}}$ (PU).

As can be seen from Table 15, the ESS acts through VIC as a load to support the frequency. Equation (38) can be used to calculate the power loss of two interconnected microgrids, and the results are 8.9×10^{-11} for the PI controller, 9.97×10^{-13} for the FOPI, $1.6 \times$

10^{-13} for the FPI, 6.4×10^{-15} for the FFOPI, and 1.6×10^{-15} for the VIC based on FFOPI. As a result, the best frequency performance and the optimal power flow are achieved in the case of the VIC based on FFOPI during the disturbance of disconnecting the tie line.

Based on the analysis of the total power loss at each disturbance, the magnitude of the total power loss of two interconnected microgrids at disconnected tie line disturbance is smaller than the magnitude of the total power loss at wind speed disturbance and solar radiation disturbance due to the lossless power of the tie line in the event of a disconnected tie line disturbance.

8. Conclusions and Perspectives

The need for clean but intermittent energy sources, as well as for power, is increasing in growing countries. Power delivery that is reliable and constant is extremely difficult. The use of microgrids has been suggested as a solution to the problem of grid outages. There were two types of microgrids taken into consideration, one without diesel engine support and the other with diesel engine support. The microgrid M_1 was without diesel engine support, while the microgrid M_2 had diesel engine support. An AC short transmission line was used to connect these two microgrids. It was suggested that additional power produced in M_2 is transmitted to M_1 to maintain a steady supply of electricity for the group of villages represented by M_2. Photovoltaic (PV) modules, a WECS, and biogas gensets are all forms of renewable energy sources found in the microgrids M_1 and M_2. In order to achieve optimal power management in two AC interconnected microgrids and to improve frequency stability, VIC was used to compensate for the lack of inertia using a power injection mechanism through a multi-objective function when subjected to different disturbances of wind speed variation, solar radiation variation, load variation, and generation contingencies. The paper investigated how to tune PI, FOPI, FPI, FPI, FFOPI, and VIC based on FFOPI controllers using PSO to mitigate frequency and voltage oscillation.

Power imbalances between generated and consumed energy can result from variations in wind, solar, and other energy sources, which can affect the microgrid's frequency and power management. The inertia of the BG, the virtual inertia of the inverter connected to the PVS, and a WECS in the absence of VIC all work together to balance out the energy imbalance. But when VIC is present, the compensatory method used in the absence of VIC is followed by the ESS's virtual inertia control, with the ESS acting as a load to support the frequency. The best power-sharing between each generating unit is used in each controller to compensate for the power differential during disturbances through a multi-objective function, with the smallest value being recorded for total power loss in the case of VIC based on FFOPI controller, compared to the other controllers, due to the minimum value of power sharing (ΔP_{IC} and ΔQ_{IC}) through the tie line at the VIC case. The results demonstrate that, in comparison to the other controllers, the VIC based on FFOPI controller achieves the greatest frequency performance and the optimal power flow.

The dynamics of the system can be significantly impacted by the severity of contingencies. Due to the inertia of the BG and virtual inertia of the inverter connected to the PVSS and WECS of each microgrid in the case of an outage of the tie line, an outage of the tie line without VIC affects microgrid stability but not a factor in microgrid instability. The VIC based on FFOPI controller provided a reaction that is superior in terms of frequency enhancement and optimal power management compared to the other controllers. However, using the ESS could enhance the stability during the disturbance period until the BG's isochronous governor responds to return the frequency to steady-state. The power imbalance during contingency disturbance is balanced by the optimal power-sharing of each generation unit at each controller through a multi-objective function which supported the minimum total power loss in the case of the VIC based on FFOPI controller.

The voltages and frequencies of both microgrids fluctuate within the allowable limits and then settle with zero steady-state error following a disturbance within 0.5s with less overshoots/undershoots (3.7e-5/−0.12e-3) using FFOPI based on VIC, which validates the

technical feasibility of the model and VIC technique. The power loss of two interconnected microgrids recorded 7.5×10^{-9} in the case of the PI controller, 2.7×10^{-9} in the case of the FOPI, 1.6×10^{-11} in the case of the FPI, 7.3×10^{-12} in the case of the FFOPI, and 7.1×10^{-14} in the case of the VIC based on FFOPI due to the minimum value of power sharing (ΔP_{IC} and ΔQ_{IC}) through the tie line at the VIC case for solar radiation disturbance. The magnitude of the total power loss of two interconnected microgrids recorded the smallest value, 1.6e-15, in the case of the VIC based on FFOPI controller due to the lossless power of the tie line in the event of a disconnected tie line disturbance. As a result, when compared to other controllers, the VIC based on FFOPI controller showed a superior response in terms of frequency improvement and ideal power management.

Institutional Review Board Statement: Not applicable.

Informed Consent Statement: Not applicable.

Data Availability Statement: Not applicable.

Conflicts of Interest: The authors declare no conflict of interest.

Glossary

List of Symbols

P_{LD}, Q_{LD}	Active and reactive power demand, respectively
P_W, Q_W	Active and reactive power generation from a WECS, respectively
P_{inW}	Controlled active power generation from a WECS
V_{inW}, θ_{inw}	Controlled voltage and voltage angle generation from a WECS, respectively
P_{DE}, Q_{DE}	Active and reactive power supply from a diesel engine, respectively
P_{PV}, Q_{PV}	Active and reactive power supply from a photovoltaic system, respectively
P_{inPV}	Controlled active power generation from a SPVS
V_{inPV}, θ_{inPV}	Controlled voltage and voltage angle generation from a SPVS, respectively
V_1, θ_1	Reference voltage and reference voltage angle for M$_1$
V_2, θ_2	Reference voltage and reference voltage angle for M$_2$
ϕ_{12}	Difference between the voltage angles of bus 1 and bus 2
X_{DE}	Internal reactance of a diesel engine
P_{BG}, Q_{BG}	Active and reactive power supply from a biogas genset, respectively
P_{IC}, Q_{IC}	Active and reactive power inflow through interconnection to the microgrid, respectively
K_{FS}, T_{FS}	Gain and time constants of the system real power, respectively.
K_{VS}, T_{VS}	Gain and time constants of the system reactive power, respectively
D_{FS}, F_{FS}	Damping coefficient of the real and reactive power, respectively
T_{WS}, T_{PVS}	Time constants of the WECS and SPV systems, respectively
X_{TWS}, X_{TPV}	Thevenin equivalent reactance of the WECS and SPV, respectively
X_d, X'_d	Direct axis synchronous reactance and transient reactance of thelternator, respectively
T'_{d0}	Direct axis open-circuit transient time constant
T_{B1}, T_{B2}, T_{B3}	Time constants of speed governor, actuator, and engine

T_{AB}, K_{AB}	Voltage regulator time constant and gain constant, respectively
T_{EB}, K_{EB}	Exciter time constant and gain constant, respectively
T_{FB}, K_{FB}	Stabilizer circuit time constant and gain constant, respectively

List of Abbreviation

RES	Renewable energy system
PCC	Point of common coupling
VSG	Virtual synchronous generator
ESS	Energy storage system
WECS	Wind energy converting system
SPVS	Solar photovoltaic system
BG	Bio-gas genset
DE	Diesel engine
PMSG	Permeant magnet synchronous generator
SLD	Single line diagram
SS	Stability study
DPLM	Distribution power loss minimization
VIC	Virtual inertia control
FFOPID	Fuzzy fractional order PID
PSO	Particle swarm optimization
ITSE	Integral time square error
OF	Objective function based on Equation (39)

Appendix A

According to the load and generation values given in Section 2, all the parameters have been calculated and listed in this appendix section with the time and gain constants that have been used to solve the model.

Microgrid 1 parameters

$$D_{FS} = \frac{\partial P_L}{\partial f} = \frac{P_L}{P_R * F} = 0.03 \; PU. \, kW \, / \, Hz$$

$$K_{FS} = \frac{1}{D_{FS}} = 88.46 \; Hz/PU. \, kW \quad T_{FS} = 15s$$

$$D_{VS} = \frac{\partial Q_L}{\partial V} = \frac{Q_L}{Q_R * V} = \frac{P_L}{P_R * F} = 0.57 \; PU. \, kVAR/PU. \, kV$$

$$K_{VS} = \frac{1}{D_{VS}} = 1.77 \; PU. \, kV/PU. \, kVAR \quad T_{VS} = 0.002513s$$

Table A1. Microgrid 1 parameters values.

Biogas1	WECS1	SPVS1
P_{BG} = 0.3043 pu Q_{BG} = 0.1473 pu	P_W = 0.1739 pu Q_W = 0.2126 pu	P_{pv} = 0.1304 pu Q_{pv} = 0.1621 pu
X_d = 1 pu X'_d = 0.15 pu T'_{d0} = 5 s T_B = 0.75 s T_{B1} = 0.01 s T_{B2} = 0.02 s T_{B3} = 0.15 s T_{B4} = 0.2 s T_{B5} = 0.014 T_{B6} = 0.04 s T_{B7} = 0.036 s K_{AB} = 200 T_{AB} = 0.05 s K_{EB} = 1 T_{EB} = 2 s K_{FB} = 0.5 T_{FB} = 1 s K_{1B} = 0.15 K_{2B} = 0.846 K_{3B} = 2.86 K_{4B} = −3.039	X_{TWS} = 0.36 pu T_W = 1 s T_{W1} = 0.001 s K_{W1} = 2.99 K_{W2} = 2.99 K_{W3} = 0.161 K_{W4} = 0.17 K_{W5} = −0.17 K_{W6} = −0.17 K_{W7} = 2.124 K_{W8} = −2.57	X_{TPVS} = 0.36 pu T_{PV} = 0.001 s K_{PV1} = 2.94 K_{PV2} = 2.94 K_{PV3} = 0.12 K_{PV4} = 0.13 K_{PV5} = −0.13 K_{PV6} = −0.13 K_{PV7} = 2.78 K_{PV8} = −2.61

Microgrid 2 parameters

$$D_{FS} = \frac{\partial P_L}{\partial f} = \frac{P_L}{P_R * F} = 0.0133 \; PU. \, kW \, / \, Hz$$

$$K_{FS} = \frac{1}{D_{FS}} = 75 \ Hz/PU.kW \quad T_{FS} = 15s$$

$$D_{VS} = \frac{\partial Q_L}{\partial V} = \frac{Q_L}{Q_R * V} = \frac{P_L}{P_R * F} = 0.67 \ PU.kVAR/PU.kV$$

$$K_{VS} = \frac{1}{D_{VS}} = 1.5 \ PU.kV/PU.kVAR \quad T_{VS} = 0.00212s$$

Table A2. Microgrid 2 parameters values.

Biogas2	WECS2	SPVS2
P_{BG} = 0.2062 pu Q_{BG} = 0.0998 pu	P_W = 0.1333 pu Q_W = 0.1658 pu	P_{pv} = 0.1304 pu Q_{pv} = 0.1621 pu
X_d = 1 pu X'_d = 0.15 pu T'_{d0} = 5 s T_B = 0.75 s T_{B1} = 0.01 s T_{B2} = 0.02 s T_{B3} = 0.15 s T_{B4} = 0.2 s T_{B5} = 0.014s T_{B6} = 0.04 s T_{B7} = 0.036 s K_{AB} = 200 T_{AB} = 0.05 s K_{EB} = 1 T_{EB} = 2 s K_{FB} = 0.5 T_{FB} = 1 s K_{1B} = 0.15 K_{2B} = 0.847 K_{3B} = 2.44 K_{4B} = −2.34	X_{TWS} = 0.47 pu T_W = 1 s T_{W1} = 0.001 s K_{W1} = 2.99 K_{W2} = 2.293 K_{W3} = 0.123 K_{W4} = −0.133 K_{W5} = −0.133 K_{W6} = −0.13 K_{W7} = 2.12 K_{W8} = −1.96	X_{TPVS} = 0.36 pu T_{PV} = 0.001 s K_{PV1} = 2.25 K_{PV2} = 2.25 K_{PV3} = 0.094 K_{PV4} = 0.1 K_{PV5} = −0.1 K_{PV6} = −0.1 K_{PV7} = 2.13 K_{PV8} = −2

Table A3. Diesel engine and AC tie line parameters values.

DE	Interconnection Data
P_{DE} = 0.2 pu Q_{DE} = 0.09686 pu	R = 0.05 pu X = 0.00676 pu P_{RES} = 50 KW P_{IRES} = 40.6 KW
K_{1DE} = −2.874 K_{2DE} = 0.2	P_{loss} = 9.39 KW K_1 = 19.68 K_2 = −19.61 K_3 = 2.364 K_4 = 2.364
K_{3DE} = 0.2 K_{4DE} = −2.681	K_5 = −2.95 K_6 = −19.68

References

1. Farrokhabadi, M.; Cañizares, C.A.; Simpson-Porco, J.W.; Nasr, E.; Fan, L.; Mendoza-Araya, P.A.; Tonkoski, R.; Tamrakar, U.; Hatziargyriou, N.; Lagos, D. Microgrid Stability Definitions, Analysis, and Examples. *IEEE Trans. Power Syst.* **2020**, *35*, 13–29.
2. Kundur, P.; Paserba, J.; Vittal, V.; Andersson, G. Closure of. Definition and Classification of Power System Stability. *IEEE Trans. Power Syst.* **2006**, *21*, 446.
3. Firdaus, A.; Sharma, D.; Mishra, S. Dynamic power flow based simplified transfer function model to study instability of low-frequency modes in inverter-based microgrids. *IET Gener. Transm. Distrib.* **2020**, *14*, 5634–5645.
4. El-Fergany, A.A.; El-Hameed, M.A. Efficient frequency controllers for autonomous two-area hybrid microgrid system using social-spider optimizer. *IET Gener. Transm. Distrib.* **2017**, *11*, 637–648.
5. Rosini, A. Power Sharing in Droop Controlled Microgrids. In Proceedings of the 2019 IEEE 11th International Symposium on Advanced Topics in Electrical Engineering (ATEE), Bucharest, Romania, 28–30 March 2019.
6. Delavari, H.; Naderian, S. Backstepping fractional sliding mode voltage control of an islanded microgrid. *IET Gener. Transm. Distrib.* **2019**, *13*, 2464–2473.
7. Jayawardana, A.; Agalgaonkar, A.P.; Robinson, D.A.; Fiorentina, M. Optimization framework for the operation of battery storage within solar-rich microgrids. *IET Smart Grid* **2019**, *2*, 504–513.
8. Sharma, R.; Kewat, S.; Singh, B. Robust MMSOGI-FLL control algorithm for power quality improvement of solar PV-SyRG pico hydro-BES based islanded microgrid with dynamic load. *IET Power Electron.* **2020**, *13*, 2874–2884.
9. Barik, A.K.; Das, D.C. Expeditious frequency control of solar photovoltaic/biogas/biodiesel generator based isolated renewable microgrid using grasshopper optimization algorithm. *IET Renew. Power Gener.* **2018**, *12*, 1659–1667.
10. Rezkallah, M.; Singh, S.; Chandra, A.; Singh, B.; Tremblay, M.; Saad, M.; Geng, H. Comprehensive Controller Implementation for Wind-PV-Diesel Based Standalone Microgrid. *IEEE Trans. Ind. Appl.* **2019**, *55*, 5416–5428.
11. Sheng, S.; Zhang, J. Capacity configuration optimization for stand-alone micro-grid based on an improved binary bat algorithm. *J. Eng.* **2017**, *13*, 2083–2087.
12. Puchalapalli, S.; Tiwari, S.K.; Singh, B.; Goel, P.K. A Microgrid Based on Wind-Driven DFIG, DG, and Solar PV Array for Optimal Fuel Consumption. *IEEE Trans. Ind. Appl.* **2020**, *56*, 4689–4699.
13. Liang, B.; Kang, L.; He, J.; Zheng, F.; Xia, Y.; Zhang, Z.; Zhang, Z.; Liu, G.; Zhao, Y. Coordination control of hybrid AC/DC microgrid. *J. Eng.* **2019**, *16*, 3264–3269.
14. Guo, L.; Fu, X.; Zeng, J. Power Management for AC/DC Hybrid Microgrid. *Front. Energy Res.* **2021**, *9*. http://dx.doi.org/10.3389/fenrg.2021.801894

15. Zhao, D.; Qian, M.; Ma, J.; Yamashita, K. Photovoltaic generator model for power system dynamic studies. *Sol. Energy* **2020**, *210*, 101–114.

16. Chao, P.; Li, W.; Liang, X.; Shuai, Y.; Sun, F.; Ge, Y. A comprehensive review on dynamic equivalent modeling of large photovoltaic power plants. *Sol. Energy*. **2020**, *210*, 87–100.

17. Yaramasu, V.; Wu, B.; Sen, P.C.; Kouro, S.; Narimani, M. High-power wind energy conversion systems: State of- the-art and emerging technologies. *Proc. IEEE.* **2015**, *103*, 740–788.

18. Gencer, A. Modelling and analysis of operation PMSG based WECS under different load conditions. In Proceedings of the 2016 IEEE 8th International Conference on Electronics, Computers and Artificial Intelligence (ECAI), Ploiesti, Romania, 30 June 2016–2 July 2016.

19. Xi, J.; Geng, H.; Ma, S.; Chi, Y.; Yang, G. Inertial response characteristics analysis and optimization of PMSG-based VSG-controlled WECS. *IET Renew. Power Gener.* **2018**, *12*, 1741–1747.

20. Johnson, S.C.; Rhodes, J.D.; Webber, M.E. Understanding the impact of non-synchronous wind and solar generation on grid stability and identifying mitigation pathways. *Appl. Energy* **2020**, *262*, 114492.

21. Ubilla, K.; Jimenez-Estevez, G.A.; Hernadez, R.; Reyes-Chamorro, L.; Irigoyen, C.H.; Severino, B.; Palma-Behnke, R. Smart Microgrids as a Solution for Rural Electrification Ensuring Long-Term Sustainability Through Cadastre and Business Models. *IEEE Trans. Sustain. Energy* **2014**, *5*, 1310–1318.

22. Suryakiran, B.V.; Singh, V.K.; Verma, A.; Bhatti, T.S. Stability study of integrated microgrid system. In Proceedings of the ICSCS 2018, Kollam, India, 19–20 April 2018; Springer: Singapore, 2018; Volume 837, pp. 817–825.

23. Vinit Kumar Singh; Bhamidipati Venkata Suryakiran; Ashu Verma. Modelling of a renewable energy-based AC interconnected rural microgrid system for the provision of uninterrupted power supply. *IET Energy Syst. Integr.* **2021**, *3*, 172–183.

24. Hasanzadeh, S.; Dehghan, S.M.; Khoramikia, H. Droop control method based on fuzzy adaptive virtual resistance for DC microgrids. *Int. J. Power Electron.* **2021**, *14*, 197.

25. Jiang, Y.; Yang, Y.; Tan, S.C.; Hui, S.Y.R. Distributed Sliding Mode Observer-Based Secondary Control for DC Microgrids Under Cyber-Attacks. *IEEE J. Emerg. Sel. Top. Circuits Syst.* **2020**, *11*, 144–154.

26. Deng, J.; Mao, Y.; Yang, Y. Distribution Power Loss Reduction of Standalone DC Microgrids Using Adaptive Differential Evolution-Based Control for Distributed Battery Systems. *Energies* **2020**, *13*, 2129.

27. Yang, Y.; Qin, Y.; Tan, S.C.; Hui, S.Y.R. Efficient Improvement of Photovoltaic-Battery Systems in Standalone DC Microgrids Using a Local Hierarchical Control for the Battery System. *IEEE Trans. Power Electron.* **2019**, *34*, 10796–10807.

28. Yang, Y.; Qin, Y.; Tan, S.C.; Hui, S.Y.R. Reducing Distribution Power Loss of Islanded AC Microgrids Using Distributed Electric Springs with Predictive Control. *IEEE Trans. Ind. Electron.* **2020**, *67*, 9001–9011.

29. Qian, X.; Yang, Y.; Li, C.; Tan, S.C. Operating Cost Reduction of DC Microgrids Under Real-Time Pricing Using Adaptive Differential Evolution Algorithm. *IEEE Access* **2020**, *8*, 169247–169258.

30. Dabbaghjamanesh, M.; Kavousi-Fard, A.; Mehraeen, S.; Zhang, J.; Dong, Z.Y. Sensitivity Analysis of Renewable Energy Integration on Stochastic Energy Management of Automated Reconfigurable Hybrid AC–DC Microgrid Considering DLR Security Constraint. *IEEE Trans. Ind. Inform.* **2020**, *16*, 120–131.

31. Yuan, Y.; Wang, D.; Liu, F.; Deng; Chen, Z. Efficiency-Prioritized Droop Control Strategy of AC Microgrid. *IEEE J. Emerg. Sel. Top. Power Electron.* **2020**, *9*, 2936–2950.

32. Wang, Y.; Zhao, Q.; Wang, X. An Asynchronous Gradient Descent Based Method for Distributed Resource Allocation with Bounded Variables. *IEEE Trans. Autom. Control* **2021**, *1*. https://doi.org/10.1109/tac.2021.3131557.

33. Boyd, S.; Vandenberghe, L. *Convex Optimization*; Cambridge Univ. Press: Cambridge, UK, 2004.

34. Boicea, V.A. Energy Storage Technologies. The Past and the Present. *Proc. IEEE* **2014**, *102*, 1777–1794.

35. Fawzy, A.; Bakeer, A.; Magdy, G.; Atawi, I.E.; Roshdy, M. Adaptive Virtual Inertia-Damping System Based on Model Predictive Control for Low-Inertia Microgrids. *IEEE Access* **2021**, *9*, 109718–109731.

36. Vorobev, P.; Huang, P.H.; Hosani, M.A.; Kirtley, J.L.; Turitsyn, K. A framework for development of universal rules for microgrids stability and control. In Proceedings of the 2017 IEEE 56th Annual Conference on Decision and Control (CDC), Melbourne, Australia, 12–15 December 2017; pp. 12–15.

37. Jiang, Y.; Pates, R.; Mallada, E. Dynamic Droop Control in Low-inertia Power Systems. *IEEE Trans. Autom. Control* **2020**, *66*, 3518–3533.

38. Ojo, Y.; Watson, J.; Lestas, I. A review of Reduced-Order Models for Microgrids: Simplifications vs Accuracy. *arXiv* **2020**, arXiv:2003.04923.

39. Abubakr, H.; Mohamed, T.H.; Hussein, M.M.; Guerrero, J.M.; Agundis-Tinajero, G. Adaptive frequency regulation strategy in multi-area microgrids including renewable energy and electric vehicles supported by virtual inertia. *Int. J. Electr. Power Energy Syst.* **2021**, *129*, 106814.

40. Kerdphol, T.; Rahman, F.S.; Watanabe, M.; Mitani, Y. *Virtual Inertia Synthesis and Control*; Springer International Publishing: Cham, Switzerland, 2021.

41. Tamrakar, U.; Shrestha, D.; Maharjan, M.; Bhattarai, B.; Hansen, T.; Tonkoski, R. Virtual Inertia: Current Trends and Future Directions. *Appl. Sci.* **2017**, *7*, 654.

42. Akinyele, D.; Belikov, J.; Levron, Y. Challenges of Microgrids in Remote Communities: A STEEP Model Application. *Energies* **2018**, *11*, 432.

43.　Hashemi, S.M.; Vahidinasab, V. *Energy Management Systems for Microgrids*; Springer International Publishing: Berlin/Heidelberg, Germany, 2021; pp. 61–95.

44.　Singh, D.; Seethalekshmi, K.A. Review on Various Virtual Inertia Techniques for Distributed Generation. In Proceedings of the IEEE International Conference on Electrical and Electronics Engineering, Gorakhpur, India, 14–15 February *2020*; pp. 14–15.

45.　Fernández-Guillamón, E.; Gómez-Lázaro, E.; Muljadi; Molina-García, Á. Power systems with high renewable energy sources: A review of inertia and frequency control strategies over time. *Renew. Sustain. Energy Rev.* **2019**, *115*, 109369.

46.　Mohamed, M.M., El Zoghby, H.M., Sharaf, S.M. and Mosa, M.A. Optimal virtual synchronous generator control of battery/supercapacitor hybrid energy storage system for frequency response enhancement of photovoltaic/diesel microgrid. *J. Energy Storage* **2022**, *51*, 104317.

47.　Ghany Mohamed Abdel Ghany, M.A.; Bensenouci, A.; Bensenouci, M.A.; Nazih Syed-Ahmad, M. Fuzzy Fractional-Order PID Tuned via Relative Rate Observer for the Egyptian Load Frequency Regulation. In Proceedings of the IEEE 2018 Twentieth International Middle East Power Systems Conference (MEPCON), Cairo, Egypt, 18–20 December 2018; pp. 18–20.

48.　Elnozahy, A.; Yousef, AM.; Ghoneim, SS.; Abdelwahab, SA.; Mohamed, M.; Abo-Elyousr, FK. Optimal Economic and Environmental Indices for Hybrid PV/Wind-Based Battery Storage System. *J. Electr. Eng. Technol.* **2021**, *16*, 2847–2862.